PhotoMOB: Automated GIS method for estimation of fractional grain dynamics in gravel bed rivers.

Part 1: Grain size

A Preprint

October 26, 2023

Fanny Ville [1], **Damià Vericat** [1,2], **Ramon. J. Batalla** [1,3], **Colin. D. Rennie** [4]

[1]Fluvial Dynamics Research Group (RIUS), University of Lleida, Lleida, Spain

[2]Forest Sciences and Technology Centre of Catalonia, Solsona, Spain

[3]Hydrological Processes Area, Catalan Institute for Water Research, Girona, Spain

[4]Department of Civil Engineering, University of Ottawa, Ottawa, Ontario, Canada

Contact details of the corresponding author:

Fanny Ville, University of Lleida, Alcalde Rovira Roure, 191, E-25198 Lleida, Catalunya, Spain

Email: fanny.ville@udl.cat

Abstract

Particle entrainment intensity is spatially and temporally variable, making it a complex phenomenon to measure. This paper is the first of a pair, in which we present an automated image processing procedure (*PhotoMOB*) for monitoring the mobility/stability of gravel river beds. The method is based on local comparison of the shape of the grains identified at the same coordinates between successive photos to identify coincident and new grains. For each grain fraction, the proportion of grains that remained immobile and the proportion of grains newly identified in the study area can be calculated. In this part 1 paper, we present only the GIS-based procedure for identifying and characterising grain shapes in digital images of bed patches to derive a reliable surface Grain Size Distribution (GSD), and for subsequent analyses of bed mobility. The procedure is compatible with different forms of sampling (Area-by-Number i.e., AbN, and Grid-by-Number i.e., GbN) and types of measurements (*continuous* or real measures of the axes and *discrete* square holes measurements of the axes). The performance of the GIS procedure is evaluated by comparing estimated percentiles against manually delineated grains in ten 40x40cm image samples, as well as against the real bed grain sizes from the same patches measured with a Pebble-Box (*continuous* axis value) and two samples measured with a template (*discrete* axis value). Under optimal condition, the average root mean squared error (RMSE) of the manual procedure compared to the real measurement is 8.2% in AbN and 16.3% in GbN, while *PhotoMOB* performance is similar with RMSE of 9.5% in AbN and 16.6% in GbN. The paper also analyses how the tool performs when compared to *discrete* procedures such as measurement with templates. We found that in AbN, the under-estimation of the apparent size due to the imbrication effect is of the same order of magnitude as the under-estimation of the grain size measured by template. In GbN form, results emphasize the need of converting grain axis as a function of the average grain flatness for compatibility with *discrete* measurement, as coarse grains have more weight in the distribution and are often flatter in shape, hence are more often retained in inferior classes than smaller more spherical particles. A sufficiently large and appropriate sample area could reduce all the above mentioned RMSE by a third for AbN and by half in GbN.

Keywords: Photographic-method, Image processing, GIS, Grain delineation , Area- and Grid-by-Number

1 Introduction

Bed-material dynamics (mobility or stability), is a process controlled by different factors, notably, bed structure, sediment supply, flow hydraulics, and bed texture, i.e., the shape, size and the position of the grains that compose the river bed (e.g., Dietrich et al., 1989; Church et al., 1998; Cassel et al., 2021; Deal et al., 2023). Depending on the importance and combination of these factors, and the history of stress (e.g., Ockelford, 2011; Mao, 2012, 2018; Ockelford and Haynes, 2013; Ockelford et al., 2019), gravel riverbeds can be subject to varying degrees of mobility in time and space. This makes it a complicated process to measure and qualify. A common indirect method of tracing grain dynamics consists of painting a surface area of the bed and then surveying after a hydrological event. This method avoids alteration of the natural packing of the particles without limitation of the size of the traced grain. If entrained painted particles can be located downstream, then transport distances can also be measured (e.g., Church and Hassan, 1992; Hassan and Ergenzinger, 2003; Mao et al., 2017; Brenna et al., 2019; Vázquez-Tarrío and Batalla, 2019; Vericat et al., 2020). However, this technique has several limitations (see Text S.1), among which is that a large amount of information from the original patch location is not further analysed such as the proportion and size of immobile particles. A solution can be to compare successive images of the bed surface taken at the same location (Vericat et al., 2008; Cerney, 2010; Peckarsky et al., 2014). Information related to grain dynamics can be extracted by a spatial grain-by-grain inter-analysis of the particles present in the two photographs. In this case, a semi- or fully-automated image processing procedure is extremely useful. This enables photographing and subsequent analysis of many different areas of the bed, such that the spatial and temporal variability of bed particle entrainment and transport can be examined. As far as we know this has not been yet fully developed. Until now, several automated procedures have been developed only for detecting particles in images and measuring them to extract the Grain Size Distribution (GSD) of the photographed surface (e.g., Ibbeken and Schleyer, 1986; Butler et al., 2001; Sime and Ferguson, 2003; Graham et al., 2005a, 2005b; Chang and Chung, 2012; Detert and Weitbrecht, 2013; Purinton and Bookhagen, 2019).

We present in this pair of papers, a GIS-based photographic processing procedure *PhotoMOB* for first characterizing the grain-size of the surface bed-materials (this paper i.e., Part 1) and quantify the changes in bed surface sediments (texture) for individual targeted patches and individual and/or sequential hydrological events. We do not aim to merely promote a new automatic image processing procedure for extracting the GSD of gravel bed river surfaces, but to go one step further. We developed a second part to determine the proportion of the bed disturbed and grain mobility by fractions (Part 2; Ville et al. 2023). Instead of estimating the transport distance of recovered tagged particles, this method focuses on a given square of a bed with the objective of quantifying for each grain fraction, the proportion of grains (number or area) that has remained stationary and the proportion that is occupied by particles that were not originally detected in this area. In addition, new particles deposited on the study surface will be included in the analysis of the next hydrological event without having made additional effort in the field other than the acquisition of a new photo.

This initial paper presents the workflow under GIS environment to perform grain shape identification and characterisation. The tool is capable of deriving *continuous* reliable surface grain size distributions (GSD) in Area-by-Number (AbN) (i.e., a number of grains on a given area) as well as in a Grid-by-Number form (i.e., sampling of a predetermined number of grains according to a grid of sampling points), and also a *discrete* size measurement that can be compared to pebble count data (Wolman, 1954). We present the results of an evaluation of the performances with a photo-set showing different characteristics of surface heterogeneity (i.e., grain size, lithology, painted or unpainted grains, direct sunlight or shaded, wet or dry particles). The performances of *PhotoMOB* are discussed and compared with the ones obtained with other available tools. Finally, we address the limits of the method as well as the compatibility of the obtained results with other non-photographic methods. In the course of this article, all the references to "Text **S**", and "Figure **S**" followed by a number indicate the location of the element in question in the supplementary information.

2 The PhotoMOB workflow

Figure 1 represents the entire workflow of the *PhotoMOB* GIS toolbox. The objective of the procedure is to identify and characterise the grains observed in a photo and, ultimately, to simply compare two photos, of the exact same bed area, acquired before and after a hydrological period in order to estimate fractional grain dynamics. The first stage Figure 1 B consists of scaling the photos and then detecting and characterising each particle in the images (i.e., size, shape and orientation characteristics). This allows extraction, Figure 1 C, of the grain size distribution, the cumulative distribution as well as percentiles, distribution of grains' orientation, proportion of the area occupied by fine material (the finest limit is defined by the operator). Only a brief presentation of the procedure will be given here. The reader is invited to read the supplementary material Text S.2 for a detailed view of the developed procedure. The second part, Figure 1 D, represented by the shaded area and fully developed in the companion paper (Part 2, Ville et al. (2023b)), consists in comparing the two photos, called here, pre (T0) and post-event (T1) photos. The shape (area, *a*-axis and *b*-axis) of each grain positioned between the two photos at the same coordinates are compared in order to classify them as possibly identical (i.e., immobile particle) or not (i.e., particle is different between images and therefore indicates new particle). This grain-by-grain analysis allows an estimate of the proportion of the bed was disturbed and the fractional mobility within the patch Figure 1 E.

2.1 Image collection

Once a sufficiently large target area has been selected, a frame (see Text S.2.1) with known exact internal dimensions is placed on the riverbed to delineate the area. The distance between each internal corner will be used to locally scale the images. The photo is recommended to be taken facing against the flow direction, with nadir view (perpendicular to the riverbed), and with the area protected from direct sunlight to avoid brightness changes within the photo. In general, the more homogeneous the area is in terms of light and colour, the easier is to detect the particles automatically. Finally, the positions of the four corners of the frame can be marked and/or surveyed by a topographic method to enable finding again the location for a subsequent photo collection. Once the area is re-visited, the frame is placed back on the bed, and the second photo is taken following the same protocol. This last field phase can be repeated for the same area successively according to successive flow events (as show in Figure 1 A).

2.2 Bed particle detection and characterisation

Once the pre- and post-event photos have been acquired, the objective of the first part of the GIS procedure is the transformation of the images (i.e., raster data type) into vector data layers (polygon type), reproducing the contour of each particle present on the photos. In this manuscript, we use the words segmentation, digitalization, delimitation and delineation as synonyms. This process is based on the assumption that the boundaries between particles correspond to the darkest pixels in the image, Figure 1 B1. Grain detection and characterization is done in five steps represented also in Figure 1 B : image pre-processing (B.1), and the image processing steps of image classification (B.2), image binarization (B.3), boundary adjustment (B.4), and grain characterization (B.5).

2.2.1 Image pre-processing

In order to facilitate good detection of the particles, the photos are first filtered externally to GIS in GIMP (Team, 2019), a free image manipulation software, to smooth the intra-grain noise while preserving edges. Afterwards, the filtered images are loaded into GIS. The four internal corners of the frame are marked manually and used as local reference points to scale the photo and correct the perspective of the image by applying a projective transformation. Finally, the second (or post-event) photo has to be aligned manually with the first one with a further projective transformation. All of these steps are developed in much greater detail in Text S.2.2.1 .

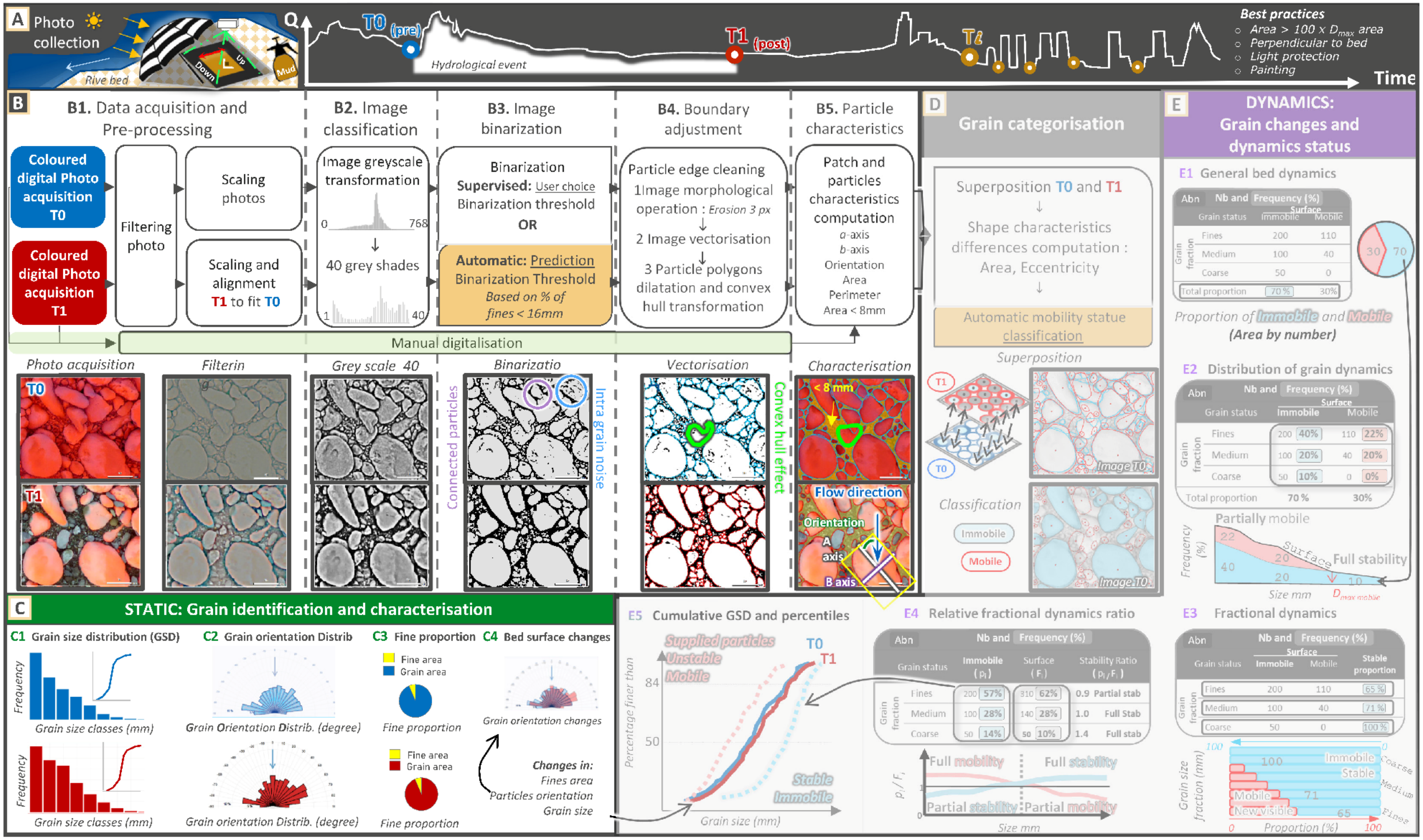

Figure 1: Illustration of the entire workflow required to sample and characterise the bed surface (developed in this paper) and sediment dynamics (shaded blocks representing what will be further analysed in Part 2, see companion paper Ville et al., 2023). (A) Photo acquisition. (B) Extraction of grain and patch characteristics. (C) Possible output after patch surface characterisation. (D) Characterisation of grain dynamics and (E) possible output from characterisation. The yellow boxes represent the developed models (i) of dark threshold prediction (see text) and (ii) of particle classification. Note the effect of the convex hull transformation on the green particle in the center of the two images in the Vectorisation and Characterisation columns. In the Characterisation column, the second image shows the sketch explaining how particle characteristics are derived.

2.2.2 Image processing

In this section we only briefly present the steps, all the thresholds and precise parameters are available in Text S.2.2.2. The scaled filtered images are transformed into a grey scale image (intensity level). Then these grey scale images have to be transformed into binary images, where the foreground would correspond to the particles (high intensity, white) and the background to the boundary of the particles and gaps (low intensity, black). To generate this binarization, a *threshold of dark intensity* must be selected to perform the partition. The selection of the threshold value to partition the image is based on the method of moments thus relies on use of the histogram of the frequency distribution of the grey levels of the pixels Figure 1 B3. The whole process can be *supervised* by the operator or be performed *automatically* through a threshold prediction model developed in this study. A fully detailed description of the prediction model is available in Text S.2.2.3. The prediction is based on a visual approximation of the areal proportion of material finer than pebbles (<16 mm) covering the study area correlated with the optimal grey level binarization threshold.

This model was trained on 67 photos representing three different light and colour conditions (C1: painted, C2: not painted, C3: not painted and with light variation) with a total of 34246 grains manually digitalized to extract the % area finer than 16 mm. In parallel, each of the same images was processed in the tool. For each of them, 22 threshold grey levels were tested, not taken as an absolute value but relative to the mean of the pixel distribution, and a single operator selected the one that provided the best segmentation. Figure 2 C shows the prediction models of the binarization threshold established with these pairs of information. A validation set of 11 patches photographed in the three conditions with proportions of area below 16 mm ranging from 15% to 71% was collected. The mean absolute error of prediction (average distance between the model line and the validation point for each photo condition on Figure 2 C was 1 grey level for photo conditions C1 and C2, but 2 grey levels for C3.

Then, the white pixel areas are converted from raster to polygons, vector features, yielding the outline of each particle Figure 1 B4. A succession of boundary adjustments and a convex envelope are applied. An example can be seen between the images in Figure 1 B4 Vectorisation and Figure 1 B5, which present the raw delimitation and the convex envelope (note the highlighted particle in the center). Once this convex hull is generated, it is possible to extract six characteristics of the patch. The (i) area and (ii) perimeter of each detected particle are directly acquired from the convex hull. For (iii) the longest axis (*a*-axis) and (iv) the intermediate axis (*b*-axis), on each particle, a minimum bounding rectangle box delimiting its smallest width is generated. The length of this rectangle corresponds to an estimate of the particle's *a*-axis, while its width corresponds to the particle's *b*-axis. Furthermore, the angle of the longest axis with north gives us information about (v) the orientation of the particle (see Figure 1 B5). Finally, (vi) an estimate of the area covered by fine material is obtained by subtracting from the total study area the summed area of particles with *b*-axis larger than a fine limit specified by the operator (by default 8mm).

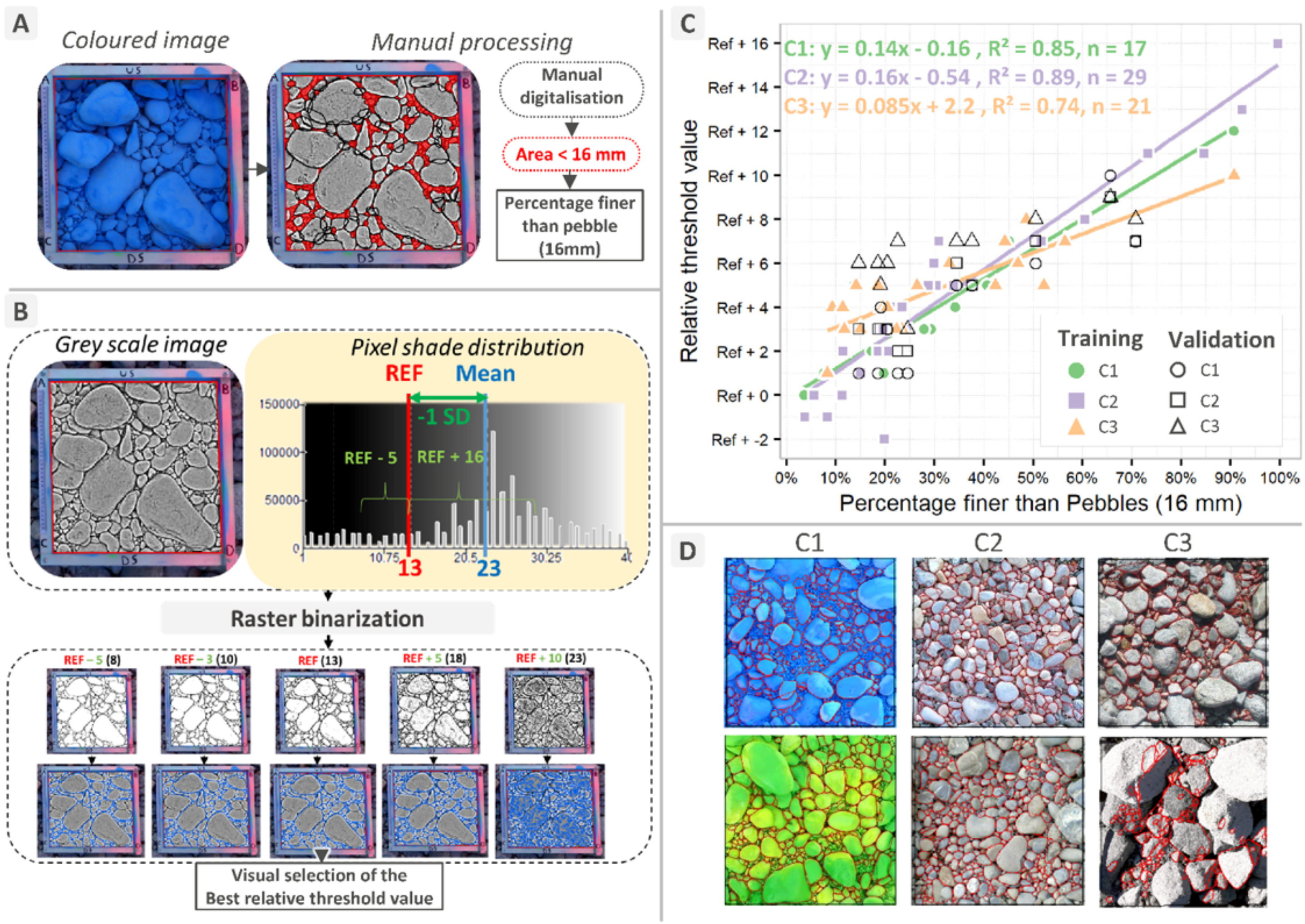

Figure 2: Training data sets used to build the dark threshold prediction model for the 3 photo conditions (n=68). (A) Percentage area covered by particles finer than pebbles derived from manual digitisation. (B) Relative value of binarisation threshold tested (22) and visual selection of the best threshold leading to an optimal delineation to build the (C) threshold prediction model for the 3 photo conditions. (D) Example of grain delineation generated by the best selected threshold for the 3 photo conditions and from different river beds.

3 Method of performances and compatibility assessment

Two questions guide the performance analysis:
(1) How good is the automatic detection of objects (grain) in the image? For this, we will compare the GSDs from the automated segmentation results, with GSDs from manual digitalization (what we consider the *gold standard*, the best we can expect for grain identification).

(2) How well do the manual and automated procedures reproduce the grains present on the surface of the bed? That is, the combined error of the segmentation procedure developed here and the errors inherent in the photographic method. To do this, we will compare the GSDs of grains identified (automatically or manually) on the images with those within the target areas extracted using the *paint-and-pick* protocol to collect all surface grains (e.g., Graham et al., 2005b) and then measured in the laboratory.

The photographic method allows sampling in the form of a number of particles (analysis method) per area (sampling method) and extracting quantitative real values (i.e., *continuous* type variables) per each grain. In order to analyse the performance of the tool, a control data set is needed, of the same form as the data to be compared (i.e., Area-by-Number (AbN)). This data set will avoid errors that would be linked to the method of data acquisition. Both manual digitalization and real data from *paint-and-pick* corresponds to AbN form (Bunte and Abt, 2001) and were preferred to grid sampling of digitalized grain on the images or the common pebble count method (Wolman, 1954) corresponding to a Grid-by-Number form (GbN).

Additionally, to the above-mentioned questions, the analysis of the compatibility of data from the photographic method with other forms and methods is guided by two other questions:

(3) How well the photographic method produces correct data in GbN form? We will transform the tested data from the images (manual and automatic) as well as the control data (*paint-and-pick*) from the AbN form to the GbN to evaluate the deviation between the test and control data in the latter form.

(4) How well the photographic method provides data compatible with data obtained by other non-photographic methods? Generally, of the GbN form and with *discrete* square holes measurements of the axes. The compatibility is analysed by comparing the GSD resulting from the automatic and manual image procedures extracted as GbN form with control data (*paint-and-pick* sampling) measured by a square holes template (binned *b*-axis sizes).

3.1 Control dataset

3.1.1 Control data set acquisition

A control dataset was used to evaluate the performance and reproducibility of the image processing procedure to produce corrected grain identification and associated GSD and as well as providing compatible data compare with other methods. The control dataset was obtained in two rivers of the South Central Pyrenees (Cinca and Ésera) to introduce lithological, shape, and imbrication variability. Moreover, at each site, the choice of patches to be photographed was guided to also introduce variations in general GSD (coarse, fine, intermediate) and possible factors leading to error of particle detection by creating complexity on images: e.g., partially wet surface, heterogeneous lithology.

A Panasonic DMC-TZ60EG© digital camera with a maximum image resolution of 4896 × 3672 (18 MP) was used to take the pictures perpendicular to the surface of the bed at a height of about 1.70 m from the ground, which gives an average image resolution of 0.4 mm after scaling. The detection limit of the particles was therefore on average 5.2 mm *b*-axis (ca. 13x13 pixels). Ten sediment patches of 0.16 m² square (40 cm × 40 cm) were photographed. According to Diplas and Fripp (1992) and Graham et al. (2005a) , to be able to represent an accurate GSD with a 0.16 m² area, the size of the larger *b*-axis particle should be about 40 mm. However, it is worth to remark that the aim here was not to fully represent the bed surface but to understand how well the photographic method reproduces it.

On each targeted area, a metal frame was placed and oriented in an upstream-downstream direction to (i) ensure a constant sampling area, (ii) orient the photo with respect to the flow direction, (iii) serve as a stencil for painting the area and (iv) allow scaling via the 4 inner corners of the frame. A first photo was acquired, corresponding to condition C3, and a second photo was acquired while shielding the area from direct sunlight with a beach umbrella, corresponding to photographic condition C2. Finally, the area inside the frame was painted and then photographed again while protected from direct sunlight. The latter corresponds to condition C1, expected to be optimal for *PhotoMOB* procedure. All these photographs are shown in Figure **S**2.

After taking the last picture, the metal frame was removed and all painted or semi-painted particles that were in contact with the edge were carefully collected and stored in a container. Then, all painted particles completely inside the area that were not in contact with the edges were collected and stored in a second container. Both containers were returned to the laboratory.

For each of the ten samples, the position orientation on the bed of each grain was estimated and classified into three categories based on the projection of the paint on their surface (Figure 3). Position 1 (P1) particles rest in a stable position with the longest and intermediate axes exposed on the surface and fully painted. These particles should be correctly characterized by our procedure. This position can be compared to the work of Ibbeken and Schleyer (1986) , Figure **S**2. Position 2 (P2) particles have the same orientation as P1 but are partially covered by one or more other particles. The painted surface shows the negative of other particles. In these conditions, the *b*-axis may be under-estimated and the aspect ratio distorted. However, if the hidden portion is less than half of the particle, the under-estimation will be minimal. Finally, Position 3 (P3) particles are orientated such that the surface exposure and thus paint is not projected onto the side showing the *a*- and *b*-axes. The size of the axes may be then under-estimated. Additionally, particles with only a small and light trace of paint were assumed to come from the sub-surface and were discarded.

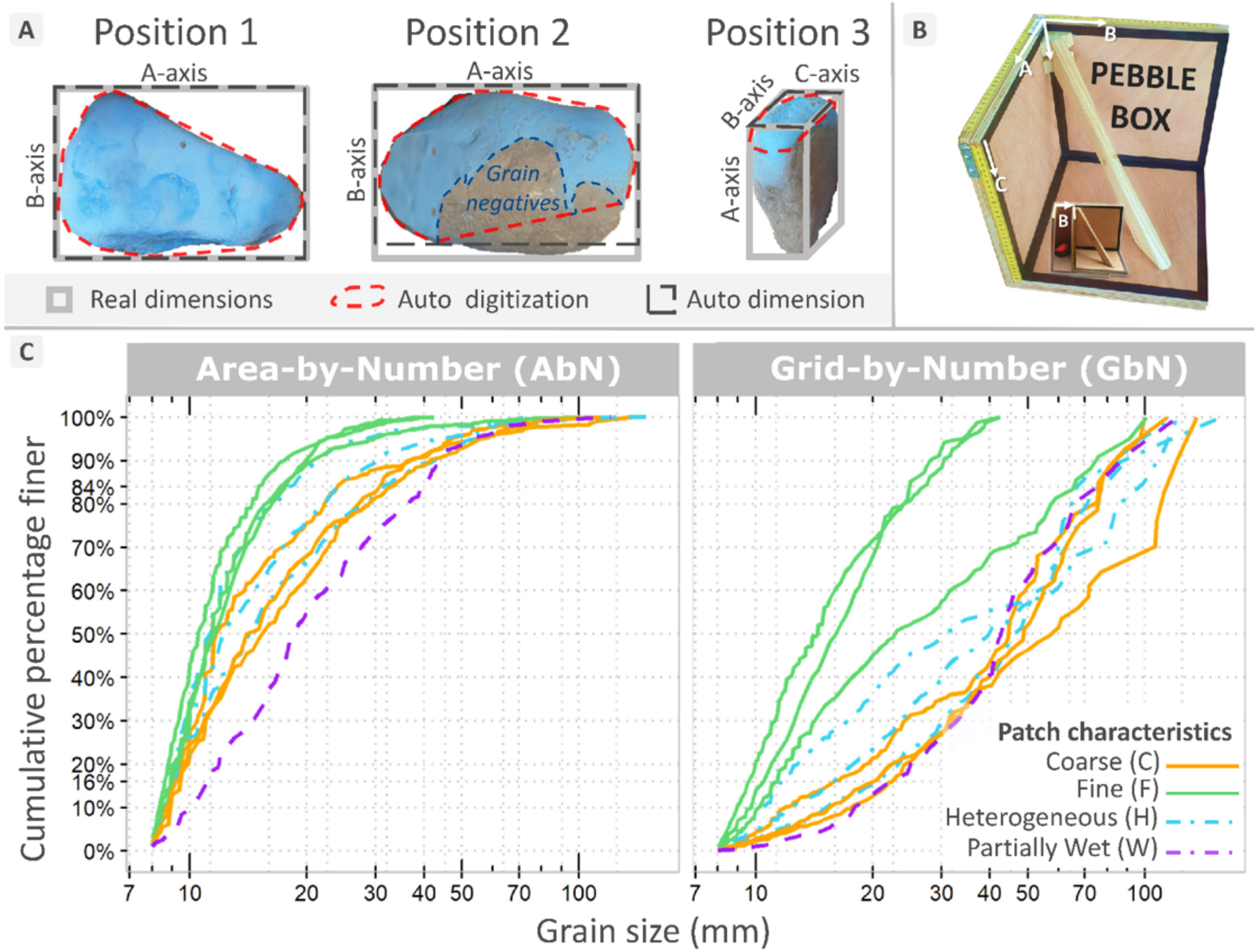

Figure 3: (A) Illustration of the position and orientation of the particles on the bed according to the projection of the paint on their surface. (B) Illustration Pebble-Box manual device (Ibbeken and Denzer, 1988) used to measure particle size axis. (C) Validation dataset used to test the particle detection image-processing procedure. Cumulative b-axis grain size distribution curves for the 10 patches and their main characteristics. Data are for AbN (*paint-and-pick* samples) truncated at 8 mm and converted to GbN using the method of Kellerhals and Bray (1971)

The actual three orthogonal axes of each particle were then measured manually using a Pebble-Box (Ibbeken and Denzer, 1988; Bunte and Abt, 2001) (*b*-axis > 8 mm) or with a caliper (*b*-axis < 8 mm). The use of the Pebble-Box Figure 3 B allows for fast and consistent measurement of the orthogonal axes as all three axes can be measured by manipulating the particle once without re-manipulating it. The accuracy of the measurement is in the range of ½ to 1 mm. About 6800 particles were manually measured and classified. In addition to being able to establish the size distribution of the *b*-axis, the measurement of the three axes allows the shape of each particle to be determined via the Zingg classification (Zingg, 1935). These samples are considered the real control grains (mentioned as *paint-and-pick* reference). Finally, for two samples, representing a total of 1000 grains, each particle, before being measured in the Pebble-Box, was passed through a template with several sieve-sized square-holes *D* with 0.5 psi -increment (psi = log2(*b*)) to obtained binned *b*-axis sizes.

3.1.2 Control data set characteristics

The characteristics of each sample are presented in Table 1, while the GSDs are presented in Figure 3 C and the particle shape and position are available in Figure **S**3. Cumulative particle size distributions are presented as Area-by-Number directly from the *paint-and-pick* sampling and also as a Grid-by-Number via the Kellerhals and Bray (1971) conversion method by multiplying the frequency of all particles-size D_i by an exponent of 2 (D_{i^2}).

The sediments of the Cinca consisted mainly of coarse-grained white granite (increasing the complexity of the photographed surface to be segmented) and pale limestone. The Ésera sediments were dominated by dark sandstone with varying degrees of metamorphism. The particle shapes of the two coarse samples S2 and S10 from this river were significantly different from the other seven with predominantly discoidal shapes (41 and 49% respectively)

The sampled patches were divided into four groups based primarily on grain size and lithology. Samples 1 through 3 were grouped as having a coarse particle size distribution (D_{50} in GbN form ranging between 44 mm to 57 mm). Samples 4 through 6, all coming from the Cinca, were grouped as having heterogeneous surfaces. Samples 4 and 5 were heterogeneous in terms of lithology, while sample 6 showed a low grain sorting coefficient (Folk and Ward, 1957) of 1.3 (poorly sorted). Samples 7 through 9 were representative of fine patches composed of between 38 and 71% material finer than pebbles (16 mm) and with D_{50} in GbN form between 14 to 22 mm. Finally, the last sample S10, was collected because it had a partially wet surface that may generate issues for grain delineation. As 49% of the sample was disc-shaped (flat and circular) and dominated at 38% by particles in position P2, it will be difficult to characterise correctly by photographic methods.

It should be noted that all samples showed a similar evolution of the median shape with increasing size (*b*-axis). The coarser the particles, the flatter they tended to be. A more complete description of these trends and of the characteristics of the control samples in general is available in the supplementary Text S.3.1.2 and Figure **S**3 .

Table 1: Sample characteristics.

	Sample	River	Fines (%)[a]	Grain number	D_{max} (mm)	Ratio: sample area/ d_{max} area	Number (nb) and frequency (%) of grains per classes										GSD form [b]	Percentiles in mm					Sorting [c]
								8 11.3	11.3 16	16 22.6	22.6 32	32 45.3	45.3 64	64 90.5	90.5 128	128 >		D5	D16	D50	D84	D95	
Coarse	S1	Cinca	15	233	136	9	*nb*	70	48	44	39	15	8	4	4	1	AbN	8.7	9.6	15.8	31.3	58.0	1.1 *Poorly*
							%	30%	21%	19%	17%	6%	3%	2%	2%	0%	GbN	12.6	22.3	57.4	113.5	128	
	S2	Ésera	19	383	114	12	*nb*	158	95	58	28	21	15	6	2		AbN	8.3	9.4	15.2	33.7	57.0	0.9 *Moderately*
							%	41%	25%	15%	7%	5%	4%	2%	1%		GbN	11.9	20.1	48.8	75.9	95.8	
	S3	Cinca	20	260	100	16	*nb*	81	63	50	21	22	15	7	1		AbN	8.5	9.3	12.0	24.4	48.1	1.1 *Poorly*
							%	31%	24%	19%	8%	8%	6%	3%	0%		GbN	10.4	15.9	44.6	77.1	97.0	
Heterogeneous	S4	Cinca	23	354	156	7	*nb*	141	82	63	38	12	13	4		1	AbN	8.4	9.0	12.7	24.8	46.4	1.1 *Poorly*
							%	40%	23%	18%	11%	3%	4%	1%		0%	GbN	10	15.9	39.7	67	117.1	
	S5	Cinca	19	313	120	11	*nb*	104	74	48	38	24	15	9	1		AbN	8.3	9.2	14.7	32.1	56.7	0.9 *Moderately*
							%	33%	24%	15%	12%	8%	5%	3%	0%		GbN	11.4	20.7	46.1	76.2	97.1	
	S6	Cinca	35	519	121	11	*nb*	259	147	70	24	7	4	5	3		AbN	8.3	9.0	11.3	18.5	28.5	1.3 *Poorly*
							%	50%	28%	13%	5%	1%	1%	1%	1%		GbN	9.3	11.7	30.8	96.6	114.8	
Fines	S7	Cinca	38	719	101	16	*nb*	348	225	87	30	15	8	4	2		AbN	8.3	9.1	11.5	17.6	30.2	1.1 *Poorly*
							%	48%	31%	12%	4%	2%	1%	1%	0%		GbN	9.2	11.3	22.8	65.4	90.9	
	S8	Cinca	71	838	42	91	*nb*	481	236	77	38	6					AbN	8.2	8.7	10.6	15.1	23.2	0.6 *Moderately well*
							%	57%	28%	9%	5%	1%					GbN	8.5	9.6	14.4	24.8	33.6	
	S9	Ésera	66	717	42.5	89	*nb*	326	232	126	23	10					AbN	8.2	9.0	12.0	18.0	22.9	
							%	45%	32%	18%	3%	1%					GbN	8.8	10.5	16	27	34.6	
Partially wet	S10	Ésera	25	203	121	11	*nb*	31	38	54	30	32	12	4	2		AbN	9.3	11.5	19.0	41.1	58.5	0.9 *Moderately*
							%	15%	19%	27%	15%	16%	6%	2%	1%		GbN	15.1	22.5	42.6	74.9	101.5	

[a]Areal fraction finer than pebbles (16mm) obtained my manual digitalisation (see Figure 2), [b] Grain size distribution in Area-by-Number form (AbN) (*paint-and-pick* samples) truncated at 8 mm and converted to Grid-by-Number (GbN) using the method of Kellerhals and Bray (1971). [c]Sorting from Folk and Ward (1957) on GbN distribution.

3.2 PhotoMOB assessment

3.2.1 Assembling of the dataset

Photos of the 10 patches were scaled and digitized by hand. Manual digitization was only carried out on the photos in C1 condition. This data set is considered the best delineation that can be expected from the image i.e., the *gold standard*. Sometimes some grains were partially covered by others to a small extent, so their presumed shape was drawn.

In order to evaluate the performance of our image processing procedures (*supervised* or *automated*) on different photographic conditions, the 30 photos (10 samples × 3 photographic conditions) were (i) processed in a *supervised* way (selection of the best binarization threshold by the same operator) and (ii) processed automatically. The automatic form of this procedure requires an estimation of the areal proportion of material finer than pebbles in the image as mentioned in Section 2.2.2 and Text S.2.2.3. By manual digitization, the proportion of the sampling area composed of particles finer than 16 mm is known. But to account for the fact that the user would need to estimate this proportion, we made a survey form asking to a total of 335 random participants the surface proportion of fine material (<16 mm) on 20 photos from the dataset corresponding to conditions C1 and C2 (the survey is available here). The mean accuracy error (MAE) of the 335 participants is 15% in C1 and 13.5% in C2 with a similar standard deviation for both conditions (14%). We processed the photos automatically by assuming for the proportion of material finer than pebbles (<16 mm) the median of the respondents' estimates for C1 and C2. We used the responses from C2 to process the photos in condition C3. The particles identified at the edge were removed from the analysis due to the metallic frame visible in the photographs. Only grains entirely within the frame were retained for the purpose of this performance analysis to allow a comparison with the *paint-and-pick* on the same exact grain population.

Figure 4 presents an overview of the digitization results obtained in a *supervised* manner (i.e., using the segmentation tool but with the binarization threshold selected by the operator) in the three photographic conditions (columns) for a sample from each group (rows). Some particles are left out of the count (labelled U_e) because they are under-segmented (i.e., joined to other particles) and bounded by a polygon touching the edges. In other cases, over-segmentations can be generated because of image complexity (intra grain colour variation). The more the photographic condition deteriorates (from C1 to C3), the more anomalies appear. This image is discussed more in Text S.3.2.1.

To allow for comparison, the 30 photos were also additionally processed through two other available tools to derive GSDs from imagery, *Basegrain*^{TM} a free and stand-alone tool developed by Detert and Weitbrecht (2013) , and *Sedimetrics Digital Gravelometer*^{TM}software (Graham et al., 2005a, 2005b). Both tools were applied using the default parameters.

The data were homogenized via truncation at 8 mm when assessing the performance of the procedures, as for each photo and each procedure the lower limit of particle detection may vary slightly. In addition, truncation eliminates from the control data set very small particles that may originate from the subsurface rather than the surface. Additionally, particles smaller than 8 mm were not measured with the Pebble-Box but with a calliper, which makes these measurements less reliable.

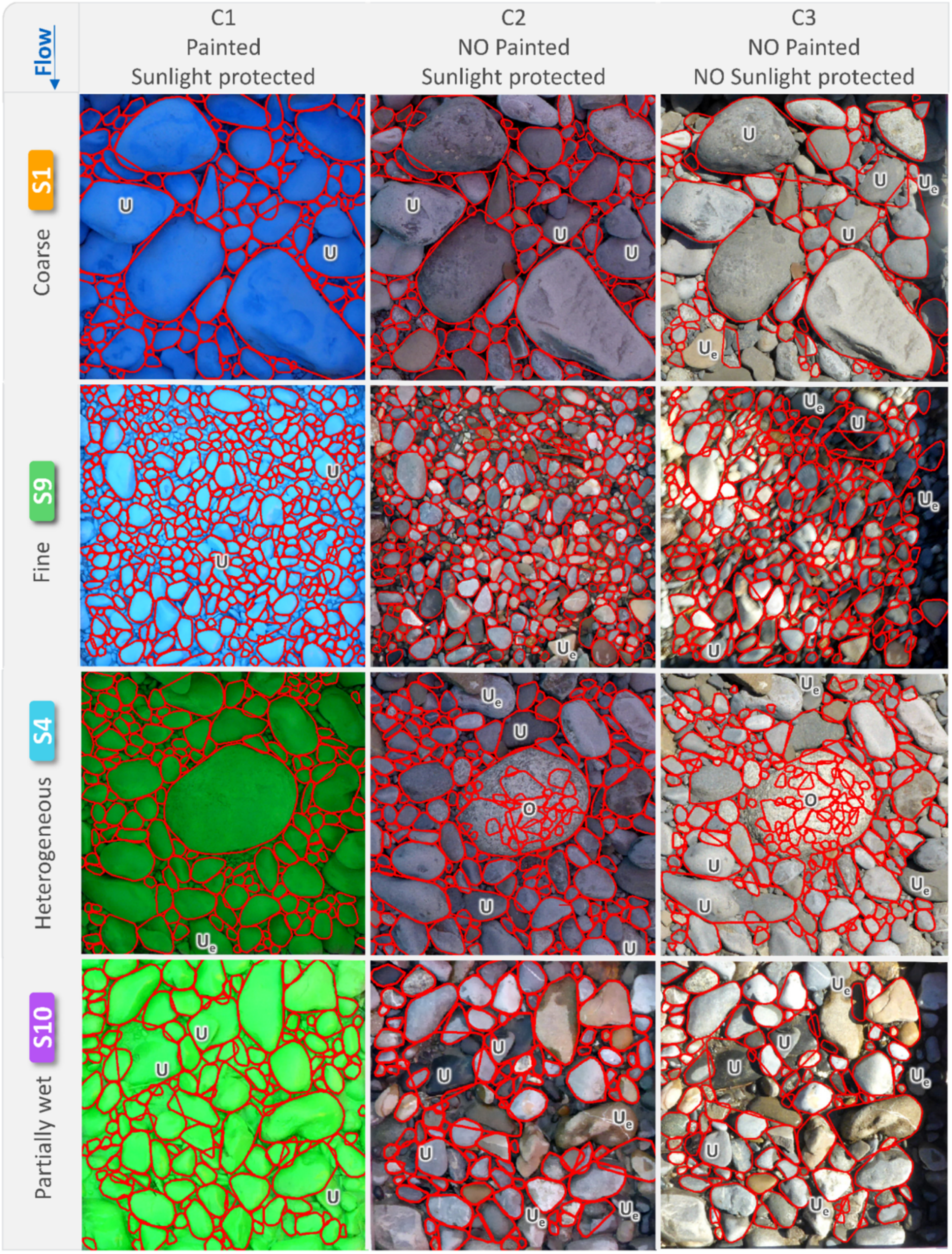

Figure 4: Particle detection results by *supervised* image-processing procedure. The 4 main patch characteristics (from top to bottom: coarse, fine, heterogeneous, partially wet) are represented for each of the 3 photographic conditions. The image patches represent approximatively 40cm×40cm and show detected particles >8mm. The 'U' label denotes examples of under-segmentation issues, the 'O' label denotes examples of over-segmentation issues and the label "U_e" denotes examples of under-segmentation leading to *non-real* large particles along the edge that were thus subsequently not taken into account.

3.2.2 GSD computation and percentiles extraction

3.2.2.1 Continuous measurement or real measure of grain For each of the 30 images (10 samples * 3 photo conditions), a real GSD (*paint-and-pick* grains collection followed by Pebble-Box axis measurements), a manual digitized distribution (*gold standard*), and four estimated distributions by each of the automated image processing procedures (*PhotoMOB* either *supervised* or *automated*, *Basegrain* and *Sedimetrics*) of *continuous* measurement are available in AbN and GbN form. It should be noted that the cumulative distribution and percentile estimates are calculated from *continuous* *b*-axis data and not, as is usually the case, from *discrete* size class data (i.e., binned *b*-axis sizes). The method of percentiles extraction in the form of Area-by-Number (number of grains of identical *b*-axis size) and Grid-by-Number (summed grain area of identical *b*-axis size), following the principles explained by Bunte and Abt (2001) and Graham et al. (2012), is fully described in section Text S.3.2.2.1. Also, this supplementary section describes examples of limitations for the GbN GSD. More analyses are also developed in Section 4.2.1 and Section 4.2.2 of this paper.

3.2.2.2 Discrete measurements or binned b-axis sizes For the 2 samples, sampled in AbN form (*paint-and-pick* protocol), but with particles also measured by the template (*discrete* square holes measurement of the axes), the extraction of percentiles for the GSDs was carried out using the common method indicated by Bunte and Abt (2001) . The conversion to the GbN form was carried out according to the Kellerhals and Bray (1971) conversion method by multiplying the frequency of all particles-size D_i by an exponent of 2 (D_{i^2}).

3.2.3 Performance and compatibility assessment

From the 360 *continuous* grain size distributions [6 procedures (real, manual, 4 automated) × 10 samples × 3 photo conditions × 2 GSD forms] and 72 *discrete* grain size distribution (6 procedures × 2 samples × 3 photo conditions × 2 GSD forms) , we extracted 2 variables, (i) Nb_i, the number of grains per grain fraction, with *i* being the lower limit in mm from each 0.5 psi unit interval grain size class [where psi=$\log_2$(b), where *b* is the size of the *b*-axis in mm] and (ii) $D_{i,}$ corresponding to15 percentiles of grain diameters in millimetres, (*i* indicates percentile number, $D_{5,10\ ,16\ ,20\ ,25\ ,30\ ,40\ ,50\ ,60\ ,70\ ,\ 75\ ,80\ ,84\ ,95}$). We will only present the results that we consider to be of interest to the community.

The residuals and the relative residuals between the estimated *i*-values and the control *i*-values for each combination between the photographic condition (C1, C2, C3), the GSD form (AbN or GbN), and the type of measurement (*continuous* or *discrete*) were computed. The relative residuals express the error of the estimated variable *i* as a percentage of the control variable *i* (manual or real).

Following Sime and Ferguson (2003) and Buscombe (2013) , using the residuals, four metrics were applied to quantify the estimation error and relative estimation error for each individual *Nb*$_i$ and D$_i$. The *bias (B)*, indicating whether the evaluations were on average over- or under-estimated, is defined as:

$$B_{Var\,i} = \frac{1}{n}\sum(Residuals_i) \tag{1}$$

where n represents the number of patches (10). The mean absolute error (MAE), corresponding to the reducible error or the error of accuracy, indicating how far from the correct value are the estimates, is given as:

$$MAE_{Var\,i} = \frac{1}{n}\sum(|Residuals_i|)) \tag{2}$$

The root means square error, representing the combination of the systematic error (bias) and the random error (irreducible random error) is calculated as:

$$RMSE_{Var\,i} = \frac{1}{n}\sum\sqrt{(Residuals_i)^2)} \tag{3}$$

And the precision error denoting the dispersion around the bias, also called irreducible random error, is:

$$e_{Var\,i} = \sqrt{RMSE_i^2 - B_i^2} \tag{4}$$

Finally, the general error of the procedures with respect to the control data (manual digitization or *paint-and-pick)* was quantified by calculating for the four above mentioned metrics, its average over all percentiles:

$$Procedure\,performance_{metrics} = \frac{1}{n} * \sum(Metrics_{D_5} + Metrics_{D_{10}} + ... + Metrics_{D_{95}}) \tag{5}$$

where n represents the number of studied percentiles (15).

4 Results and discussion

4.1 Performances

4.1.1 Grain's detection - Comparison to manual grain distribution or Gold standard

Figure 5 presents the bias, accuracy and precision for each photo condition (rows) to reproduce the manual delineation. The performances of each procedure, obtained from Equation 5, are shown in Table 2. Figure 5 A displays the mean bias of grain number detection per grain size class for our *supervised* and *automated* procedures as well as for *Basegrain* and *Sedimetrics* procedures. The vertical shaded areas mark the 10% error limits. The curves in Figure 5 B represent the relative bias (%) along the percentiles estimates (an average curve passing between the residuals in Figure 5 C for each procedure. Figure 5 C shows the dispersion of the 10 relative residuals for the 15 percentiles estimates. The shape and colour of the dots represent the 4 groups of samples. Finally, part D of Figure 5 illustrates, for the 4 procedures compared to manual delineation, the average accuracy and precision error obtained for each individual percentile (coloured dots) as well as the overall performance of each procedure (black square, values reported in Table 2). On the ordinate is the relative MAE (%) for each percentile, i.e., the mean absolute deviation of the residuals from the grey line of equality in parts B and C, while on the abscissa is the irreducible error (*e*) (precision error), which indicates the dispersion of the residuals among themselves for each percentile.

4.1.1.1 Condition 1 – Painted and Sunlight protected The *supervised* and *automated PhotoMOB* procedures present similar trends concerning bias of the detected number of grains Figure 5 A, orange and green bars) and percentiles estimates compared to manual delineation. The number of particles between 8 and 16 mm is constantly under-estimated by -15% to -25% (negative bias). Grains may have shifted to lower class or discarded (detected below 8 mm) due to the contour enhancement in the pre-processing step (see Text S.2.2.1). Then from 32 mm the trends are less constant (shaded horizontal rectangles areas in Figure 5 A) but generally there is an over-detection of grain number (positive bias). Due to the low number of particles present in these fractions (see Table 1), a few erroneous particle detections will quickly lead to high percentage of error compared to the reference number. Figure 5 B first row, *supervised* and *automated PhotoMOB* (orange and green curves) shows low or no bias and then a progressive positive bias from D_{60} to D_{95} reaching +9.7% (i.e., bias of +3 mm at D_{95}). In C1 only the end of the distribution is deviated from *gold standard* due to under-segmentation (union of grains) errors creating large polygons (see Figure 4). However, all percentiles are estimated with an accuracy error and a precision error lower than 10% (all points are located in the shaded area on Figure 5 D (first row, first and second columns).

The *Basegrain* procedure is the least biased in C1 (Figure 5 B, first row, brown line) but with a higher residual dispersion than for the two *PhotoMOB* procedures Figure 5 C, first row, 3rd column). For *Sedimetrics*, grain detection is more under-estimated for fine grain classes (grey segment on Figure 5 A, first row) resulting in a positively biased percentile estimation due to the lack of small grains. (Figure 5 B, first row, grey line). The residuals are much more scattered with a general irreducible error of 9% (Figure 5, part C and D last column).

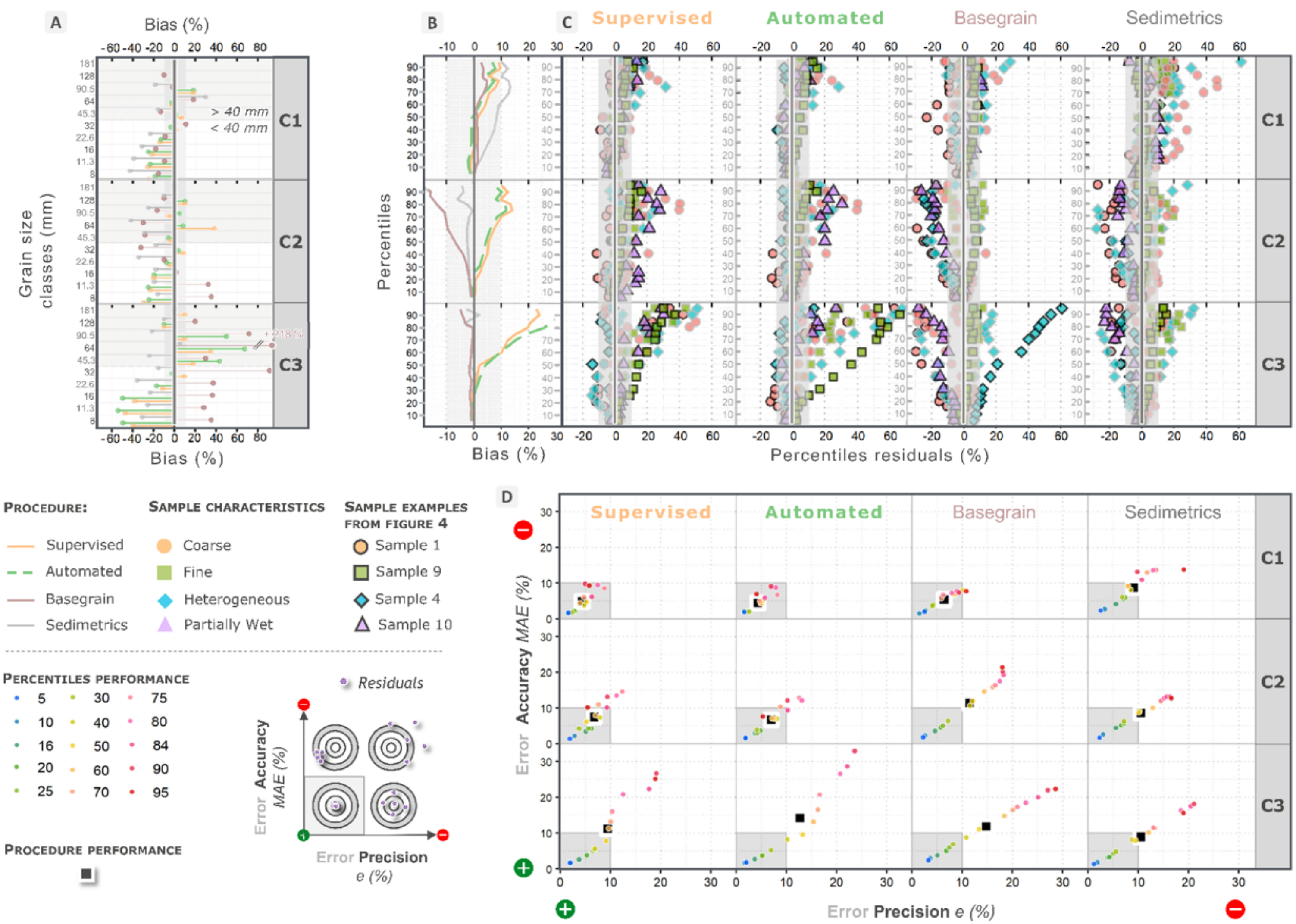

Figure 5: Performance assessment of image processing procedures compared to manual digitization (*gold standard* expected from photographic method). (A) Relative bias of grain detection number per grain size classes under the three photo conditions for the *supervised* and *automated PhotoMOB* procedure as well as for *Basegrain* free stand-alone tool from Detert and Weitbrecht (2013) and *Sedimetrics Digital Gravelometer*^{TM} from Graham (2005a, 2005b) . (B) Relative bias of percentiles estimation for each procedure. Bias is calculated over residuals of the 10 samples. (C) Distribution of the 150 relative residuals of percentiles estimation (15 percentiles * 10 samples) for the 4 automated procedures. The residuals are coloured according to the 4 main patch characteristics (coarse, fine, heterogeneous, partially wet). Samples taken as example in Figure 4 are represented here by symbols with black outline. (D) Average relative performance for the individual estimation of each percentile (coloured point) as well as the average general performance of the procedures (black square). The shaded vertical areas in A, B, C and D mark the 10% error limits.

4.1.1.2 Condition 2 – Not Painted but Sunlight protected The *supervised* and *automated PhotoMOB* procedures present, again, similar trends between them in C2 condition (second row). Grain detection is under-estimated in classes between 8 and 22.6 mm. As a reminder, for our 10 samples, between 60 and 95% of particles belong to these classes (see Figure 3). For particles larger than 22.6 mm the bias is generally low (<10%, i.e., inside shaded vertical area). Percentiles estimates are more scattered and positively biased as the percentiles increase than in C1 (Figure 5 C second row, first and second columns and Figure 5 B orange and green curves), reaching a maximum positive relative bias of 14% (i.e., +2.8 mm error on the D_{75} estimate). Then the percentile estimate bias is constant until the end of the distribution. This behaviour is due to more frequent grain union over a wider range of grain sizes, as can be seen in Figure 4. Each percentile of sample S10 is over-estimated (Figure 5 C second row, first and second column, triangle points). This is because of under-segmentation (unified grains), especially in the wet area (see Figure 4, last row), resulting in a coarser GSD.

However, *PhotoMOB* gives similar GSD to a manual digitalization, with average accuracy and precision procedure performance errors between 6.8 et 7.5% (see black squares in Figure 5 D second row ,1st and 2nd columns and Table 2. Only the percentiles of the D_{75} to D_{90} are estimated with mean errors greater than 10% (between 10 and 14.5%).

In contrast, for *Basegrain* and *Sedimetrics*, the percentiles of the sample S10 are under-estimated (Figure 5 C second row, 3rd and 4th columns, triangle points), the general percentiles bias is negative (Figure 5 B second row, brown and grey curves) and show larger disparity between the sample's residuals, also represented in Figure 5 D (second row, 3rd and 4th columns) by higher precision error or *e*. The general average precision error of these procedures is greater than 10% (black squares are outside of the shaded area).

4.1.1.3 Condition 3 – Not Painted and Not Sunlight protected In C3 (3rd row in Figure 5 A) the two *PhotoMOB* procedures differ in that the biases in the grain size estimates and the dispersion of the residual percentiles are greater for the *automated* procedure than for the *supervised* procedure. For both, procedure difference in performance between groups of samples is remarkable. Percentile precision error reaches more than 20% for high percentiles (Figure 5 D last row, 1st and 2nd columns). Sample S4 with heterogeneous lithology (blue diamonds with dark boundary) and some of the coarse samples (orange circles; S1) have under-estimated sizes (due to over segmentation) while for the other groups our procedures over-estimate the percentiles because of the creation of large coarse *non-real* or *fictitious* particles.

Basegrain and *Sedimetrics* show deviation from the *gold standard* (manual delineation) in a similar way to C2 (Figure 5 C second and last rows, 3rd and 4th columns). Their percentiles estimated average MAE are almost equal in C2 and C3 (Table 2 around 11 and 9%).

Overall, for C1 and C2 our procedures reproduce the manual GSD (*gold standard*) with a good precision and accuracy (Figure 5 D 1st and 2nd row and column) but with a tendency to over-estimate the percentiles with an average bias procedure performance of up to +6.3% Table 2. All procedures show that the error compared to manual delineation is percentile dependent, with low error for the small percentiles (blue dots in Figure 5 D and progressively larger errors for larger percentiles (red dots in Figure 5 D).

4.1.2 Photographic method performance - Comparison to real bed distribution or Paint-and-pick

The photographic method, even manual procedure, provides an estimate of GSD from a surface, where the detected particle size is limited by its visible surface. Conversely, for the *paint-and-pick* sampling, the particles are taken out of the bed to be measured. It has already been shown by previous authors that the photographic method may tend to under-estimate the real particle size distribution (Butler et al., 2001; Graham et al., 2005b; Sime and Ferguson, 2003).

Figure 6 presents the performances taking the *paint-and-pick* (i.e., real data) as the reference. Part A1 presents the dispersion of the 10 relative residuals for the 15 percentiles estimates from the *gold standard* (manual). The shape and colour of the dots represent the 4 groups of samples. The curves in Figure 6 A2 represent the relative bias (%) along the percentiles (the mean curves passing between the residuals) for the five image processing procedures in photo condition C1. The dispersion of the residuals of percentiles estimate for the four automatic procedures as well as the bias evolution under the 3 conditions are available as supplementary material Figure **S**5. Part A3 and B of Figure 6 illustrate, for the manual and for the four automated procedures, the average performance (accuracy and precision) obtained for each percentile (coloured dots) as well as the overall performances of the procedures (black square). On the ordinate is given the relative MAE (%) for each percentile, thus the absolute deviation of the residuals from the grey equality line in parts A1 and A2, while on the abscissa is represented the irreducible error (*e*, i.e., precision), denoting the dispersion of the residuals among themselves for each percentile. Finally, parts C and D present the mean bias of grain number detection per grain size class under each photo condition (rows) for automated and manual procedures respectively.

4.1.2.1 Manual delineation Figure 6 D (black segment, first row) shows that the number of grains identified in C1 by manual digitization is lower in all classes than that collected in the *paint-and-pick* samples. Classes from 8 to 22.6 mm are under-predicted with a mostly increasing trend, then from 32 mm onward the negative bias decreases with increasing size. An exception is visible in the class 64 mm where the number of particles detected is strongly negatively biased at almost -60%. This class contains many disk-shaped (flat) particles (54.5 %) leading to the class with the most particles in the P2 overlapped position (over 57%). Particles may therefore be mistakenly categorized in the smaller classes. The residuals of percentile estimates are quite clustered with the exception of sample S10 (Figure 6 A1). This is the sample which has the most discoid (flat) particles (see Figure **S**3 B and C) and for which the 11 mm (D_{20}) to 16 mm class is the most dominated (at 50%) by P3 oriented particles. Thus, all these particles will tend to be identified as finer. This has the effect of refining the distribution from the D_{20} percentiles onwards. This behaviour is not related to the partially wet nature of the sample but to the shape and position of the particles in the bed (called the fabric effect by Graham et al. (2010)). The manual bias is almost constant (Figure 6 A2 black segment). Percentiles are generally underestimated in average by -2.6% (or -0.7 mm) (see Table 2). The accuracy and precision errors over percentiles range between 2 and 13% (0.1 to 4.7 mm) (see Figure 6 A3).

Table 2: General procedure performances - Deviation from manual digitization and real measurements

Reference	Photo Condition	Procedure	Procedure Bias (B) [a]				Procedure Irreducible error (e) [a]				Procedure Accuracy error (MAE) [a]				Procedure RMSE [a]			
			mm	(sd)	%	(sd)	mm	(sd)	%	(sd)	mm	(sd)	%	(sd)	mm	(sd)	%	(sd)
Manual digitization [b]	C1	Supervised	0.9	(1.2)	3.3	(4.2)	1.0	(0.9)	4.3	(2.2)	1.0	(1.1)	4.8	(3.1)	1.4	(1.4)	6.1	(3.8)
		Automatic	0.6	(0.9)	1.8	(3.8)	0.9	(0.7)	4.3	(2.3)	0.9	(0.9)	4.5	(2.5)	1.2	(1.1)	5.6	(3.1)
		Basegrain [d]	0.2	(0.3)	1.8	(1.5)	1.3	(1.1)	6.3	(3.0)	1.0	(0.8)	5.3	(2.3)	1.3	(1.1)	6.7	(3.1)
		Sedimetrics [e]	1.4	(1.2)	7.4	(4.7)	1.7	(1.5)	9.0	(4.2)	1.6	(1.4)	8.7	(4.1)	2.2	(1.9)	11.9	(5.8)
	C2	Supervised	1.3	(1.4)	6.3	(5.0)	1.4	(1.1)	6.7	(2.9)	1.5	(1.3)	7.5	(4.3)	2.0	(1.7)	9.5	(5.2)
		Automatic	1.1	(1.2)	4.6	(4.8)	1.5	(1.2)	6.9	(3.6)	1.4	(1.2)	6.8	(3.9)	1.9	(1.6)	8.8	(5.2)
		Basegrain [d]	-2.3	(2.8)	-7.8	(6.3)	2.8	(2.8)	11.4	(6.1)	2.8	(2.9)	11.4	(7.0)	3.7	(4.0)	14.0	(8.5)
		Sedimetrics [e]	-0.9	(1.0)	-2.3	(1.4)	2.5	(2.3)	10.6	(5.0)	1.9	(1.7)	8.6	(4.0)	2.6	(2.5)	10.9	(5.0)
	C3	Supervised	2.0	(2.7)	8.4	(9.9)	2.0	(2.2)	9.4	(5.6)	2.4	(2.8)	11.2	(8.9)	2.9	(3.4)	13.5	(10.2)
		Automatic	2.7	(4.2)	11.6	(14.0)	2.5	(3.0)	12.6	(8.3)	3.1	(4.0)	14.2	(12.4)	3.9	(5.0)	18.1	(15.1)
		Basegrain [d]	-0.9	(1.2)	-1.6	(1.5)	3.6	(3.9)	14.8	(9.0)	2.8	(3.0)	11.8	(7.2)	3.7	(4.1)	14.9	(9.0)
		Sedimetrics [e]	-0.6	(0.8)	-0.6	(1.3)	2.5	(2.7)	10.6	(6.9)	2.0	(2.1)	9.0	(5.9)	2.6	(2.8)	10.6	(6.9)
Paint-and-pick [c]	**Manual – Gold standard**		**-0.7**	**(0.8)**	**-2.6**	**(1.6)**	**1.9**	**(1.4)**	**7.6**	**(2.6)**	**1.3**	**(1.0)**	**5.8**	**(2.3)**	**2.0**	**(1.6)**	**8.2**	**(2.7)**
	C1	Supervised	0.1	(0.6)	0.5	(3.6)	2.1	(1.7)	8.9	(3.7)	1.5	(1.2)	6.9	(3.1)	2.2	(1.7)	9.5	(3.8)
		Automated	-0.2	(0.5)	-0.9	(3.3)	2.1	(1.6)	8.7	(3.5)	1.5	(1.2)	6.6	(2.6)	2.2	(1.5)	9.4	(3.3)
		Basegrain [d]	-0.5	(0.7)	-1.0	(1.6)	2.0	(1.7)	8.7	(3.7)	1.5	(1.4)	6.7	(3.1)	2.1	(1.8)	8.8	(3.7)
		Sedimetric [e]	0.7	(0.8)	4.6	(4.4)	2.7	(2.5)	12.1	(6.1)	2.2	(2.0)	10.1	(5.6)	2.9	(2.6)	13.2	(6.9)
	C2	Supervised	0.6	(0.9)	3.2	(4.5)	1.7	(1.5)	7.6	(4.8)	1.4	(1.2)	6.5	(3.8)	1.9	(1.7)	8.9	(5.6)
		Automated	0.4	(0.8)	1.6	(4.3)	1.8	(1.6)	8.3	(4.1)	1.3	(1.2)	6.2	(2.9)	2.0	(1.6)	9.3	(4.5)
		Basegrain [d]	-3.0	(3.5)	-10.4	(6.9)	3.2	(3.0)	11.6	(5.7)	3.2	(3.6)	12.0	(7.6)	4.4	(4.6)	15.7	(8.8)
		Sedimetric [e]	-1.6	(1.7)	-5.0	(2.2)	3.0	(2.6)	11.9	(4.9)	2.3	(2.2)	9.6	(4.3)	3.4	(3.0)	13.0	(5.1)
	C3	Supervised	1.3	(2.1)	5.4	(9.2)	2.7	(2.8)	11.4	(7.1)	2.6	(2.9)	11.5	(8.4)	3.1	(3.3)	14.1	(9.7)
		Automated	2.0	(3.5)	8.5	(13.0)	3.4	(3.7)	14.6	(9.2)	3.2	(3.8)	14.3	(11.4)	4.1	(4.9)	18.5	(13.8)
		Basegrain [d]	-1.6	(1.9)	-4.0	(2.6)	4.3	(4.1)	17.2	(8.5)	3.5	(3.4)	14.0	(7.5)	4.6	(4.5)	17.8	(8.6)
		Sedimetric [e]	-1.3	(1.5)	-3.2	(1.7)	3.2	(3.2)	12.3	(7.0)	2.4	(2.6)	9.8	(6.2)	3.5	(3.5)	12.8	(7.0)

[a] For each of the 15 extracted percentiles, the 4 performance parameters were calculated on the 10 sample residuals. Then, each of the parameters was averaged over the 15 percentiles to give a general error for the procedure estimate. The standard deviation is given to illustrate the inter percentiles estimation performance variation; [b] General deviation from manual digitization; [c] General deviation from the *paint-and-pick* bed surface sampling; [d] *Basegrain* free stand-alone tool from Detert and Weitbrecht (2013) and *Sedimetrics Digital Gravelometer*^{TM} from Graham (2005a, 2005b). Note that *Gold standard* (highlighted in orange) is based on manual digitalization and is compared with real percentiles (i.e., *paint-and-pick*).

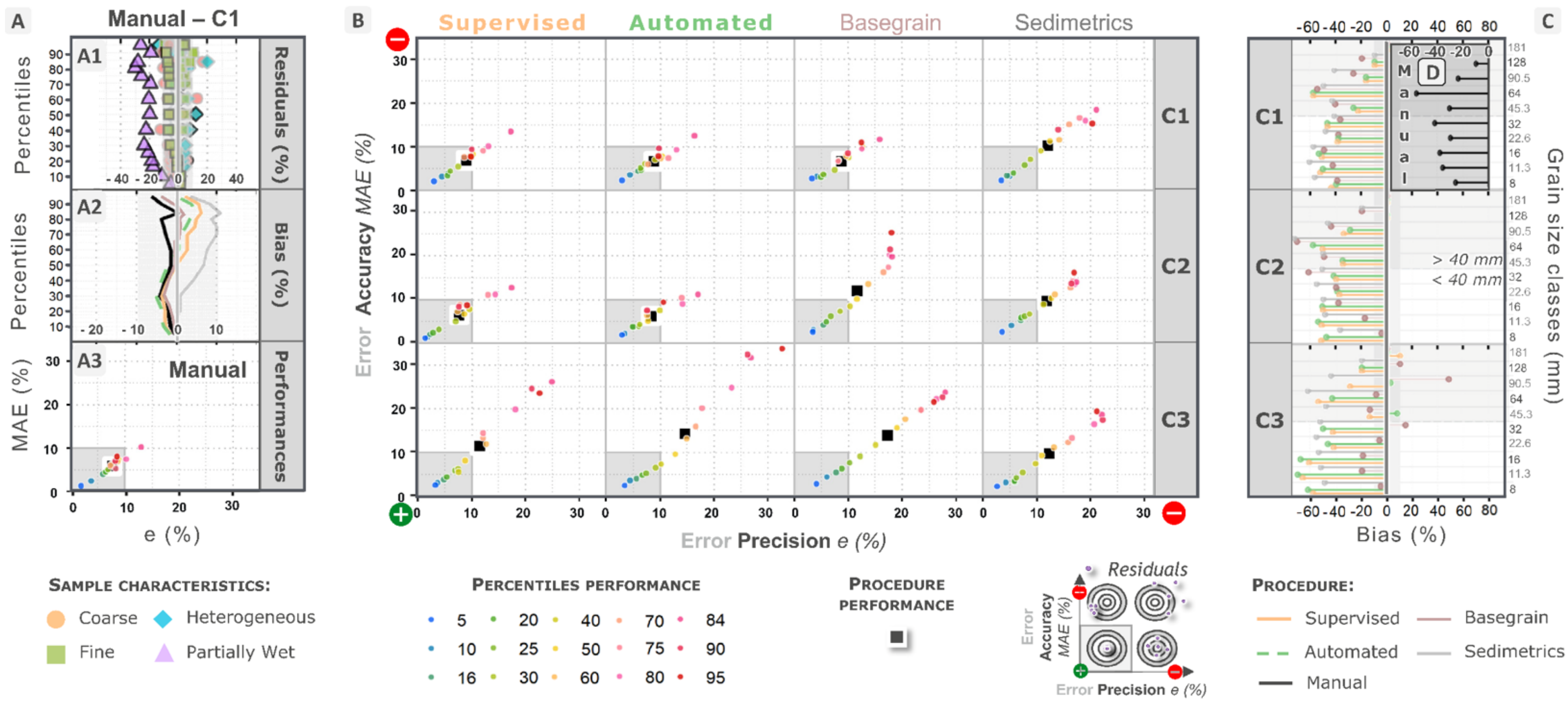

Figure 6: Performance assessment of image processing procedures compared to paint-and-pick bed surface sampling. (A) Manual digitalisation performances. Manual digitalisation was performed only on painted photos (C1). (A1) Distribution of the 10 relative residuals of each sample for the 15 percentile estimates for manual digitisation. The residuals are coloured according to the 4 main patch characteristics (coarse, fine, heterogeneous, partially wet). Samples taken as example in Figure 4 are represented here by symbols with black outlines. (A2) Relative bias of percentiles estimation in C1 photo condition for the manual procedure, the *supervised* and *automated* PhotoMOB procedures as well as for Basegrain free stand-alone tool from Detert and Weitbrecht (2013) and *Sedimetrics Digital Gravelometer*^{TM} from Graham (2005a, 2005b). Bias is calculated over residuals of the 10 samples. (A3) Average relative performance (accuracy and precision) for the estimation of each percentile (coloured dots), as well as the overall performance (black square) of manual digitalisation and (B) four automatic procedures. (C) Relative bias of grain detection number per grain size classes for the 4 image-based procedures and for the three photo conditions and (D) manual procedure. The vertical shaded areas mark the 10% error limits.

4.1.2.2 Automated delineation In C1 and C2 (Figure 6 C, 1st and 2nd rows), the *PhotoMOB* procedures show the same behaviour between them (as mentioned in section 4.1.1.1), similar to the manual procedure. There is underestimation or a negative bias of the number of particles up to 22.6 mm and then, as the size increases, the bias is reduced. As with manual delineation, there is an exception with a larger underestimate of around 60% between 64- and 90.5-mm. Figure 6 A2 shows that percentiles bias estimates are similarly negative as the manual procedure up to D_{50}, then overestimated. Percentiles from D_{70} to D_{84} are estimated with more than 10% accuracy or precision error (out of the shaded area on Figure 6 B, first row, 1st and 2nd column). This is a consequence of the union of grains (under-segmentation), which implies the appearance of *non-real* coarse grains and the diminution of finer grains in the estimated GSD. Finally, the error decreases for the D_{90} and D_{95} percentiles.

For *Basegrain*, the number of grains from 8 to 22 mm is much less under-estimated in C2 and C3 (bias only between 0 and -40%, Figure 6C 2nd and 3rd rows, brown bars) than by the other procedures, even manual (Figure 6 D). *Basegrain* over-estimates the number of grains visible on the picture due to a large amount of over-segmentation. By compensation, the bias of number of detected grains is low even if the photographic method cannot detect all the real grains present in the patch.

The average accuracy (i.e., MAE) and precision errors (i.e., irreducible error *e*) of *PhotoMOB* procedures in C1 and C2 are between 6 and 9 % (1.3 to 2 mm, Table 2). In C1 errors are basically the same magnitude as with the *Basegrain* (Figure 6 B 1st row, 1st, 2nd and 3rd columns) or the manual procedure (Figure 6 A3). In C2, our procedures are the ones with the lowest error compare to the real GSD (Table 2, Figure 6 B, second row). In C3 however, our procedures reproduce the *paint-and-pick* (real bed GSD) method with less good performance (Figure 6 B, 1st and 2nd columns, last row).

Finally, although *Sedimetrics* is the procedure that best reproduces the *paint-and-pick* method in the relatively challenging C3 condition (Figure 6 B, last row, last column), it should be noted that *Sedimetrics* had similar performance for all three photographic conditions. For all three conditions, the mean precision was around 12%, while the average accuracy was 10%. These stable results over the three conditions (Figure 6 B last column, see black square constant position) confirm that the tool developed by Graham (2005a, 2005b) performs acceptably well regardless of condition (lithology, grain texture, lighting).

4.1.3 Limitations and further developments

4.1.3.1 Limitations The *supervised* and *automated PhotoMOB* procedures have shown satisfactory performance. Average percentiles estimate error are less than 10% in both conditions C1 and C2, taking either the manual digitization (*gold standard*) or real grain size distribution as reference (Figure 5 D, and Figure 6 B 1st and 2nd rows and columns). The GSDs are relatively similar to those found by manual delimitation (i.e., *gold standard*), not due to compensation, but due to correct delimitation especially in condition C1 where image complexity (Purinton and Bookhagen, 2019) is reduced by paint, which avoids the problems caused by intra granular colour variation, veins, fractures, and shadow variations. Moreover, there was no marked difference between the different groups of samples (coarse, fine, heterogeneous, partially wet), indicating the tool can be applied to a variety of river beds.

However, in C1 and C2 we detected a positive bias for coarser particles in our *PhotoMOB* procedure. During the development of the binarization threshold process development, under-segmentation errors (union of two or more particles) were preferred to over-segmentation errors. This resulted in a greater number of coarse *non-real* or *fictitious* particles resulting, in case of C2, an over-estimated of the D_{75} to D_{84}. As the accuracy error ranges between 10 and 15% (i.e., accuracy from 90 to 85%) for these percentiles, it will not be necessary to correct the *non-real* particle delimitation if the operator accepts this margin of error in the estimation of the coarsest percentiles. However, if the GSD is to be expressed in GbN, these erroneous delimitations will have a greater weight (detailed discussion in Section 4.2.1 below), or if the user intends to use the second part of *PhotoMOB* to characterize grain dynamics (detailed in the companion paper (Ville et al., 2023b), a correction will be necessary. Poorly delineated or segmented particles will result in an over-estimation of mobile particles, because if incorrectly delineated particles overlap between the two images, even if they are the same, there is a high chance that they are classified as different (i.e., mobile or new particles). It will then be preferable to correct them. Nevertheless, these particle unions are easily visible. An operator will tend to see these very coarse visible errors more easily than fictitious small polygons (*non-real*). Finally, in C3 the prediction threshold for the binarization threshold is less performant and *PhotoMOB* was not developed to perform in this photographic condition where the use of only one binarization threshold is not suitable for images with varying intensity.

4.1.3.2 Methodological improvements for image acquisition and processing First, in C2 and C3, to avoid partially wet area issues, a solution to the problem of darker wet areas would be to humidify the whole patch to reduce the colour variation between the wet and dry areas. Correct delineation is more generally obtained with C1 type photos (e.g., painted and protected from the sun), but if it is not possible to protect the area from the sun (C3) and/or if the area cannot be painted with common spray paint (C2), several recommendations are offered here to reduce grain identification errors and the subsequent manual correction effort. In order for *PhotoMOB* to best identify grains, a first solution could be to prepare a highly concentrated simple mixture of clay and water and applied it to the bed area with a gardening spray. This reduces the complexity of the image and reflectance of the surface by its colour and matte texture.

Secondly, very recently, a new open-source software library based on convolutional neural networks, called *ImageGrains* was released by Mair et al. (Preprint EarthArXiv 2023) with the possibility in the near future to be implemented for GIS. A second solution could be to implement *ImageGrains* in the *PhotoMOB* workflow to reduce the correction effort and then carry out the second part of the protocol. We tested *ImageGrains* and *PhotoMOB* on a challenging patch containing grains with varied lithology that could cause strong over-segmentation in conditions C2 (shaded but not painted) and C1 (shaded and painted with a clay solution). The percentiles are estimated by *ImageGrains* with a bias close to 0% in both C2 and C1 compare to a manual delineation. The use of clay paint reduces the estimation bias for the *PhotoMOB* procedure from -12% to -3%. More details on these two solutions are provided in Text S.4.1.3.2 and Figure **S**6. In general, following numerous tests on different images (not presented in this paper), *ImageGrains* enables very satisfactory grain segmentations on photos taken under C3 and C2 conditions but not in C1 for which it has not been trained. In the future, it is expected to train *ImageGrains* with our painted images manually digitalized. Our digitalization will be available. Finally, as this tool seems to be flexible in terms of training, it might also be possible to train it on underwater photos. This would make it possible to track mobility, or at least the proportion of stable and perturbed bed area, even in areas that are still in the water.

Errors will always remain regardless of the procedure used (*PhotoMOB*, *Basegrain*, *Sedimetrics*, *ImageGrains*) but the two mentioned improvements could reduce drastically segmentation error and the effort of correction. As *PhotoMOB* is developed under GIS, the manual correction of persistent errors is facilitated. All the output of our image processing procedure is in the form of a vector file, which makes it easy to manipulate the results for a GIS user, hence giving a surplus of flexibility to our tool.

4.2 Compatibility with existing GbN data

4.2.1 GbN performances

Most of the existing data on GSD for more than half a century comes from a surface count of the particles via a Grid-by-Number (as Wolman method, (Wolman, 1954)) or from a subsurface volume by weight method (bulk sampling). As we pointed out in Text S.3.2.2 and Figure **S**4, Grid-by-Number form seems to be more sensitive than Area-by-Number form to over-estimation of the coarser fractions due to the low number of coarse grains present in the sample. This reflects the need to have a sufficiently large area to characterise the whole distribution correctly.

We conducted a sensitivity analysis to understand how the performance of the photographic-based procedures depend on the choice of size of the sampled area and on the distribution form, AbN or GbN. The sample area size was assessed by varying GSD truncation to vary the representation of the coarsest analysed fraction in the image (i.e., Diplas and Fripp (1992) criterion for the minimum extension of the analysed area). Specifically, we present performance calculations for (1) AbN with only a low truncation at 8 mm, as well as five other GSD forms: (2) AbN truncated between 8 mm and 40 mm (40 mm allowing to respect the Diplas criterion in accordance with the sampled area), (3) AbN with low truncation at 11 mm, (4) AbN truncated between 11.3 and 40 mm, (5) GbN with low truncation at 8 mm, and (6) GbN truncated between 8 mm and 40 mm to meet the Diplas criterion. Figure 7 A shows, for each image processing procedure, the performance average RMSE (Equation 5) calculated over the 15 percentiles mean RMSE and their standard deviation (corresponding to the last column in Table 2 but for different distribution truncation) with *paint-and-pick* measurements taken as reference. The lower the average RMSE values, the less error there is in the overall percentile estimate compared to the 'real' *paint-and-pick* data. Furthermore, the closer the values of the automatic procedures (*PhotoMOB supervised* or *automated*, *Basegrain* and *Sedimetrics*) are to the value of the manual (black) procedure, the more likely it is that the automatic delineation obtained corresponds to what the operator would expect visually.

A low truncation (8 or 11.3 mm, (1) and (3) on the X- axis) used in AbN has little influence on performance. A lower truncation at 11.3 mm (3) reduces errors by only 10% compared to an 8 mm truncation (1) regardless of the photographic condition and image procedure used. When an upper truncation (40 mm here) is used to meet the Diplas and Fripp (1992) criterion, the results get better. Average RMSEs are reduced by a third in all photographic conditions and for all procedures ((1) vs. (2) and (3) vs. (4)). It should be noted that none of our 10 samples had a ratio *area sampled/area* D_{max} >= 100 (see Table 1). In C1 and C2 our procedures (orange and green points) are very close to the manual process (black points) and remain below 10% error regardless of the truncation performed (all points are inside the shaded area). On the other hand, the errors of automated procedures under GbN GSDs with only lower truncation at 8 mm (5) are large (between 15 and 20% in C1, 15 and 35% in C2 and 25 and 50% in C3), while the use of upper truncation (6) reduces the errors to below 10% for the manual procedure and our *supervised* and *automated* procedures in C1 and C2.

Figure 7 B shows in more detail the RMSE in condition C1, for each percentile estimate between the manual delineation (*gold standard*) and the real grain size distribution (*paint-and-pick*). The respect of the criterion (i.e., ratio *area sampled/area* D_{max} >= 100) in AbN (dashed red curve compared to solid red curve) allows to reduce the error of the D_{50} estimation from 9 to 7.8% and the error on the D_{84} from 13 to 5.6%. In GbN, compliance with the criterion (black dashed curve compared to solid black curve) reduces the error of the D_{50} estimate from 17 to 5.6% and the error of the D_{84} estimate from 35 to 5.6%. The same behaviour and order of magnitude of error reduction for *PhotoMOB supervised* is showed in supplementary material S.4.2.2 and Figure **S**8.

Respecting the Diplas and Fripp (1992) criterion allows a better estimation of the percentiles and especially the largest ones (from the D_{80}). Respecting the criterion ensures the same performance whether distributions are expressed in AbN or GbN forms (black and red dashed line superposed). These specific performance gains may not be generalizable to other rivers, as here we did not perform this experiment by sampling a larger study area but by performing a truncation. However, we reiterate that if the GSDs obtained via photographic processing are to be derived in GbN form for comparison with other data or for use in sediment transport equations, then it is imperative that the extent of the photographic area is at least 100 times greater than the area of the largest grain. If the frame size is not adjustable then it may be possible to take several photographs of the site to be characterised so that the total area under study converges to the Diplas criterion and then combine all the particles identified into a single composite sample.

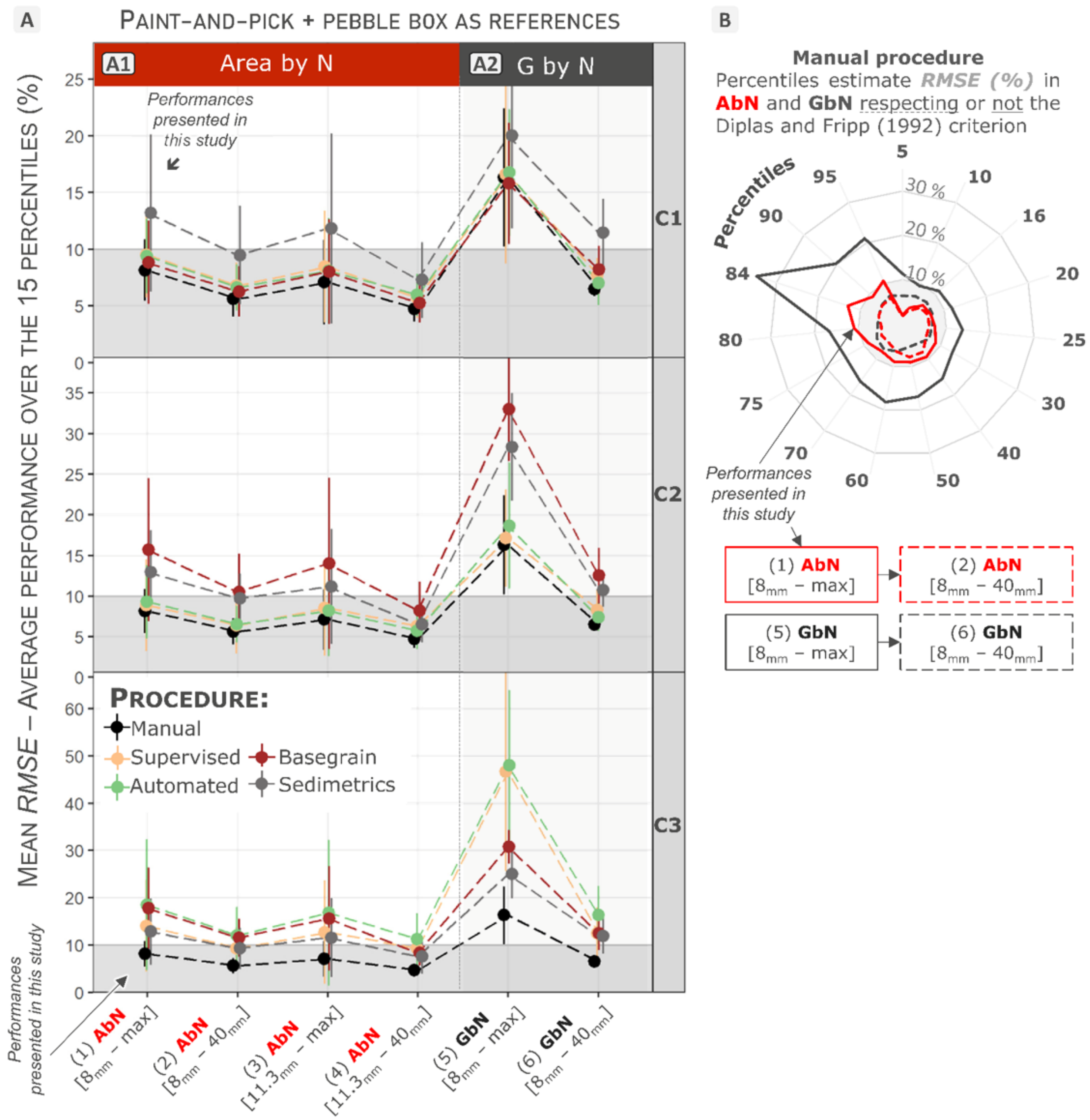

Figure 7: (A) Evolution of the overall performance of each image processing procedure as a function of low and high truncation (respecting the Diplas and Fripp (1992) criterion) in the form of (A1) Area-by-Number and (A2) Grid-by-Number. The dots represent the average RMSE of each procedure (average of the RMSEs calculated for each of the 15 percentiles estimate (based on the 10 residuals)). The bars represent the standard deviation around the mean RMSE (scatter of the RMSE of the 15 percentiles). (B) Estimate RMSE of each of the 15 percentiles from Manual delimitation (gold standard) for grain size distribution in Area-by-Number (red curves) and Grid-by-Number form (black curve) with (dashed curve) and without (solid curve) high truncation at 40mm to respect the Diplas and Fripp (1992)

4.2.2 Compatibility between continuous and discrete square holes measurements

We chose the Pebble-Box approach to measure the actual size, *b*, of each particle ≥ 8 mm, which yields *continuous real* values of the axis, as the Photographic method gives also *continuous b*-axis sizes. Most of the existing data on GSD are from surface count of the particles via a Grid-by-Number (often called Wolman count, Wolman (1954)) or from a subsurface volume-by-weigh method (bulk sampling) with *b*-axis size measured by template or sieve device. Sometimes, the only information available in GbN are a few percentiles from a previous study or from other authors where the original database is no longer available. Also, percentile could be used in sediment transport equations that have been established mostly using GbN data measured by square holes. Below we examine the compatibility of GSDs obtained from photographs with GSDs obtained from sieves or template.

For sample S2 (dominated by coarse and discoid or flat particles) and S9 (fine and spherical particles), each particle, before being measured in the Pebble-Box, was passed through a template with several sieve-sized square-holes *D* with 0.5 psi -increment (psi = $\log_2$(b)) to extract *discrete* binned *b*-axis sizes. The retained sizes recorded via the template, *D*, are influenced by the grain flatness (*c/b*) as described by Church et al. (1987) via the relationship $D/b = \frac{1}{\sqrt{2}} \times [1 + (c/b)^2]^{0.5}$. Graham (2005b, 2010) reported for 500 measured particles (*a*, *b* and *c* axes) a *D/b* ratio ranging from 0.79 to 0.82. Graham (2005b, 2010) therefore transformed the apparent *b′* axes obtained by the photographic method with a factor of 0.79 (*c/b* =0.51) and 0.8 (*c/b*=0.71) respectively in order to compare them to the control set obtained by sieving. Stähly et al. (2017), showed a *D/b* ratio ranging from 0.83 to 0.86 on 2245 clasts. Similarly, to these last authors, our 10 samples (6800 particles) show a median theoretical ratio *D/b* ranging from 0.837 to 0.892 (corresponding to a flatness index ranging from 0.634 to 0.768) with an average of 0.872. However, we noticed a significant disparity in the ratio value between particles smaller and larger than 16 mm (see Figure **S**7).

As mentioned in the description of the samples, and visible in Figure **S**3, the particles of the 8/11.3 mm and 11.3/16 mm classes, in addition to representing almost 50% or more than of the total particles (see Table 1 and Figure 3 C), are the ones with the highest flatness index while the rest of the particles (larger than 16 mm) present lower *c/b* ratios. This has the effect of under-estimating the real size *b* of the larger particles (smaller in number) by allowing them to pass through the sieve more often due to their smaller thickness. Figure 8 shows the GSD in AbN (A1) and GbN (B1) from different measurement procedures (Pebble-Box, template, manual photo-delineation) while Tables A2 and B2 in Figure 8 show the average bias (average of the 15 residual percentiles) between procedures for each sample. In both A1 and B1, the solid red curve (template GSD) is localized to the left of the black solid curve (Pebble-Box GSD), with the template GSD being 5% (15%) finer on average than the Pebble-Box GSD in AbN form (GbN form). The way the control set is measured is therefore important, and it is more or less important depending on the form of the expressed GSD (AbN or GbN).

For our two samples S2 and S9, we know the median *D/b* ratio of particles smaller and larger than 16 mm, respectively 0.843 and 0.815 for S2, 0.864 and 0.837 for S9. A binary conversion factor, one for particles < 16 mm and a second for particles > 16 mm, was used to convert the control GSD obtained from a *continuous* measurement (Pebble-Box, black dashed curve) to the control GSD obtained from sieved measurement (Template, red solid curve). In both AbN and GbN, the black dashed curve converges to the red *continuous* curve. This conversion seems to be suitable for our study sites as the average bias falls between -1% and 0% in AbN and -3 and 0% in GbN.

On the two samples S2 and S9 in AbN, Figure 8 A1, the apparent GSDs obtained by manual delineation (blue solid curve) show an under-estimation compared to the Pebble-Box (black solid curve) of about 5%, as do the GSDs obtained from the template (blue and red curve overlap quite well). The average Manual vs. Template bias varies between -1 and +1% (MAE=1%). Such observations have already been made by Stähly et al. (2017). In their study, they found a constant *b′/b* ratio (photographic apparent size *b′*/actual measured size *b*) of 0.86. Here, we found a *D/b* ratio of 0.87. Therefore, the *D/b′* ratio should be close to 1.

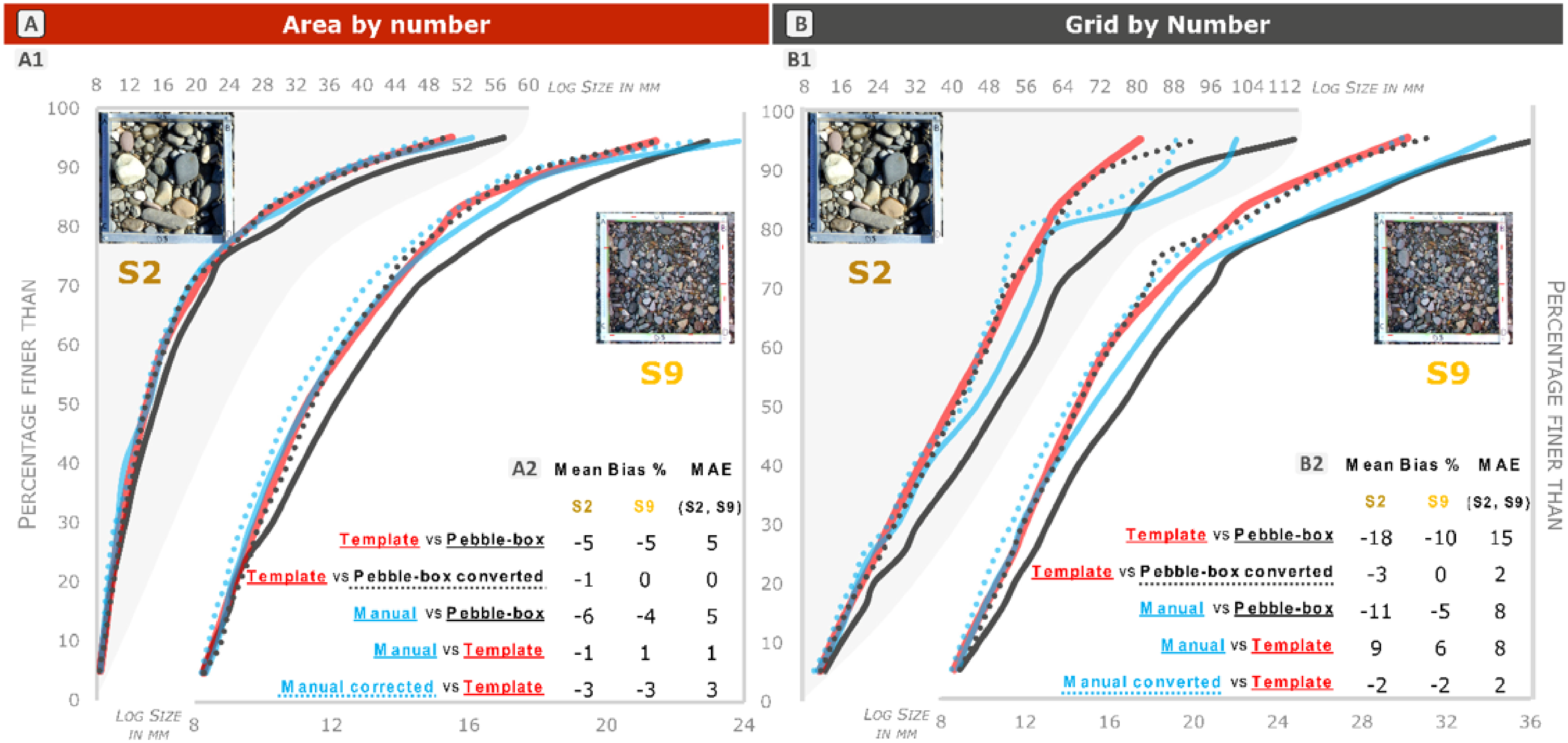

Figure 8: Comparison of the control sampling procedure (Pebble-Box or template/sieving) and its effect on the performance found for percentile estimation with the manual photographic method. Are represented as a curve, the 15 percentiles ($D_{5,10,16,20,25,30,40,50,60,70,75,80,84,95}$) in AbN form (A1) and GbN form (B1) of sample S2 and S9 according to (i) Pebble-Box measurement (black solid line), (ii) template measurement (red solid line), (iii) Pebble-Box converted to sieve form (black dashed line) via the *D/b* ratio (Church et al., 1987), (iv) manual digitisation (blue line) and (v) manual digitisation converted to sieved form (blue dashed line) via the *D/b* ratio (Church et al., 1987). In the lower right part of the plots, are annotated with corresponding colours, the mean bias over the 15 percentiles estimates with the two forms (AbN – A2 and GbN – B2) of control dataset taken as reference (Pebble-Box or template) for each sample.

This means that the impact of the fabric effect, minimising the apparent *b′* axis by photographic method compared to the real measurement (*b′/b*), is of the same order of magnitude as the reduction of the GSD by sieving compared to the real measurement *b* (*D/b*). We therefore make the same conclusion as Stähly et al. (2017), the GSD obtained by manual delineation is directly comparable to the GSD obtained by sieving. However, these conclusions are not valid in GbN. The same analyses were performed for the *supervised PhotoMOB* procedure (MAE=3%) and reach the same conclusion but not presented here for lack of space.

In GbN, the representativeness of the particles is proportional to the surface area of the grains. The shape of the GSD is therefore controlled by the largest particles (even if they are smaller in number). As these coarser particles are more often under-estimated by sieving than the fines by virtue of being flatter, the sieved GSD (retained hole size *D*) becomes finer than the apparent size from manual delimitation GSD (*b′*). The red solid curve in B1 is localized on the left of the blue solid curve whereas in A1 they were superposed. The manual GSD is on average 8% larger than the template. In this context, a conversion may be necessary if one wants to compare the photographic GSD (blue) with a sieved/template GSD (red).

It is difficult to estimate the average *D/b* ratio of each patch photographed, let alone the ratio for particles smaller than 16 mm and those larger. This would involve taking a number of particles of different sizes and measuring their *c* and *b* axes. The two-factor conversion applied here to the Pebble-Box records is actually impractical. Furthermore, the manual delineation (blue solid curve) under-estimates the GSD of the Pebble-Box (black solid curve) by about 8%. Using a binary factor, which works well to convert the Pebble-Box GSD (black dashed line) to a template/sieved GSD (red solid curve) would produce a converted manual GSD finer than the template (-6% on average, manual delimitation curve converted with double factor is not presented in this figure for better clarity). Using a factor of 0.8 as proposed by Graham et al. (2005b) would also be too large, producing a converted manual GSD finer than the template by -8% on average (manual delimitation curve converted with 0.8 factor are not presented in this figure for better clarity). Using the average *D/b* ratio of 0.87 calculated on our ten samples, allows us to reduce the bias between the manual delineation converted (blues dashed curve) and the template (red solid curve) to -2% for both samples despite their significantly different shapes and grain sizes. We have reached the same conclusion for the *PhotoMOB Supervised* procedure delineation, applying the conversion factor allows to reduce the MAE from 24% to 12%. It should be noted that for these results mentioned here, the sampled area does not meet Diplas's criterion, the distributions have not been truncated. Once truncated the percentile deviation for both manual and *supervised* procedure are of 6%. A graph summarizing the percentile RMSEs for the manual and *supervised* procedures based on GSD in AbN and GbN, without and with high truncation as well as without and with *b′* axis conversion is available in Figure **S**8 -Part B

4.2.3 Intended purpose

The acquisition of data by photographic methods and their processing must be conditioned by the use that will be made of them in order to obtain a correct level of precision in the characterisation of the real grains of the river bed. Below we list recommendations for using data from the photographic method:

(1) If the *PhotoMOB* derived GSDs are to be of *continuous* form and AbN, then they can be used as they are. The percentiles in the AbN form with the manual procedure are estimated with an average error of less than 10%. However, the percentile estimate is not constant, it is little higher than 10% for the largest percentile. A minimum area equal to 100 times the coarsest grain seems to reduce the error to about 5% in average in our case.

(2) If the *PhotoMOB* derived GSDs are to be compared with GSDs in AbN of *discrete* form obtained by sieving or passing through a template (e.g., areal sampling + sieving measurement), they can be used as they are as long as the extent area is large enough to characterise the whole grain size range. The under-estimation of grain size via photo due to the fabric effect is similar to the under-estimation of the actual grain size when measured through a template due to the degree of flatness leading which may to a classification in a lower fraction.

(3) If the *PhotoMOB* derived GSDs are to be compared with the GSDs in GbN form with *continuous* values (e.g., pebble count with a calliper to measure sizes) then the ratio of the sampled area to the area of the largest particle must be at least 100. In this study we found that, under good photographic conditions (C1), the average error in estimating the percentiles could be reduced from 15-20% to 5-10%.

(4) Finally, if the *PhotoMOB* derived GSDs are to be compared with GSDs in GbN form with *discrete* values (e.g., pebble count sampling + template measurement or bulk sample + sieving) then it will be necessary to (i) respect the criterion of a sampled area at least 100 times the size of the largest particle and (ii) convert the apparent grain size as a function of the flatness index. This will have the effect of making the GSD finer, as a sieve tends to minimise the actual grain size of particles that are relatively flat. However, a flatness index cannot be generalised to all rivers. In our case, we found that the flatness indexes used by Graham (2005b, 2010) were not suitable for our samples. A conversion factor of 0.87 for the rivers Ésera and Cinca seems to be appropriate to compare the photographic GSD with real sieved data. It may be worthwhile to sample the *c*- and *b*-axis of a sample of grains to obtain an average flatness ratio on a particular river or section. This little effort will enable more precise results to be obtained in the perspective of spatial and temporal tracking using photographic methods.

4.3 Final discussion

For several reasons, it is difficult to compare the performance data of this paper with previous authors who have already worked on this topic (e.g., Ibbeken and Schleyer, 1986; Butler et al., 2001; Sime and Ferguson, 2003; Graham et al., 2005a, 2005b; Buscombe, 2008, 2013; Warrick et al., 2009; Strom et al., 2010; Chang and Chung, 2012; Detert and Weitbrecht, 2013; Stähly et al., 2017; Purinton and Bookhagen, 2019). Many have provided (i) the results not in millimetre units but in psi units and (ii) the relative errors (%) are not always fully reported. Additionally, (iii) performance is presented for different lower truncations and sometimes, (iv) the control data set varies between a manual delimitation on a photo taken as a reference or the actual grains taken from the bed as the reference. In the latter case (v) the tested data sets were sometimes obtained in GbN form so the photographic distributions (AbN form) were converted to Grid-by-Number, by taking only a few particles from the photos along a grid or via the Kellerhals and Bray (1971) conversion method or even by the area of segmented particles as described previously in this paper with the help of Text S.3.2.2 and Figure **S**4. One last parameter makes it difficult to compare the performance with the other works mentioned above: (vi) once the real grain size constitutes the control sets, grains are systematically measured by sieving, generally square holes, and then the number of grains per particle size classes is counted, which generates *discrete* values. The percentile values are then estimated by interpolation, either linear or spline, between the particle size classes. This has a direct impact on the control distribution and, consequently, to the error estimates. If we had acquired our control set only by sieving, as almost all other studies on this topic, we would have obtained lower errors. Figure 8 showed that in AbN, the average bias of the manual delimitation was -5% with the Pebble-Box as reference, but it goes down to -1/1% when taking the GSD by sieving as reference. In GbN, the average bias of the manual delimitation was -8% with the Pebble-Box as reference, yet it goes down to -2% with the GSD by sieving as reference if the conversion factor is well adapted. So, if the authors previously cited had used a Pebble-Box, they may have found somewhat larger errors.

5 Conclusion

This paper is the first (Part 1) of a pair of connected papers in which we present an automated image processing procedure for measure grains and monitoring the mobility/stability (bed dynamics) of gravel river beds from photographs. We present here only the GIS-based procedure for identifying and measuring grains in order to derive a reliable surface Grain Size Distributions (GSD) together with additional information form the texture of the bed. The main conclusions of the paper are as follows:

(1) The *PhotoMOB* procedure identifies grain contours in a very similar way to those obtained by a manual delineation, with an efficiency to estimates percentile better or comparable to existing procedures as *Basegrain* and *Sedimetrics* when the bed area is painted and protected from the sun during photo adquisition (i.e., C1, RMSE of 6.1 – 5.6% compare to 6.7-11.9%). PhotoMOB also performs better when the bed is not painted but still protected from the sun (i.e., C2, RMSE of 9.5-8.8% compare to 14.0-10.9%).

(2) The study of the shape of the particles sampled in the Cinca and Ésera rivers showed that there is a slight tendency to flatten with increasing size between 16 and 64 mm. The coarsest sample (S10) having 60% of its grains in this size range and having the most discoidal shape and overlapped particle was most strongly under-estimated by manual delineation (on average at -20%). Therefore, in some cases, the fabric effect (shape and imbrication) on GSD accuracy may be significant.

(3) Despite the impact of the fabric effect, the photographic method provides reliable percentile estimates. Over the 10 sample studied, the manual delineation shows an RMSE of 8.2% (corresponding to an RMSE of 2 mm) in relation to the measured grain which were actually present on the surface of the bed. Similarly, *PhotoMOB* both, *supervised* and *automated*, provides RMSEs of 8.9-9.5% (around 2.2 mm) for photo conditions C1 and C2.

(3) The GSDs extracted from the photographic method (AbN sampling, *continuous* axis measures) can be compatible with different sampling and measurement methods (GbN - sieved). The 2 square holes sieved samples studied, indicate that respecting a sufficiently large sampling area to cover the whole grain size range properly and taking into account the mean grain flatness, allows an average MAE error in percentile estimation by the photographic method (manual of PhotoMOB delineation) of 6%.

(4) The use of photography allows for a reduction in field time workload, monitoring over time without artificially altering the bed surface, and the technique does not require mandatory use of aerosol paint to mark particles but can of course be coupled to particle travel distance measurements.

(5) Finally, the accuracy of the delineation not just affects the GSDs, it I also fundamental to decrease errors when paired photos are compared to analyse bed dynamics (companion paper, Part 2 by Ville et al., 2023). In order to increase the speed of the whole process and to avoid the operator having to work too hard to correct under- or over-segmented particles, the photographed area should be protected from direct sunlight and painted if possible (C1 photo condition). A future enhancement to the tool could be the use/integration of the model developed by Mair et al. (Preprint EarthArXiv 2023) into the workflow to reduce the correction effort that is working very well on C2 and C3. *PhotoMOB* has the advantage of running under GIS, making it easier for the large community of ArcGIS® users to verify, correct and manipulate the results.

Code availability

The processing of the images with the ArcGIS desktop toolbox PhotoMOB part 1 and 2 generates shapefile with for each grain, in pre- and post-event, its shape characteristics (area, perimeter, *a*-axis, *b*-axis, orientation, rectangularity, eccentricity, roundness, compactness) as well as its classification (immobile/mobile). The attribute table of these layers is also saved in text format. A web and desktop application based on R language and shiny package (R Core Team, 2022; Chang et al., 2023), called PhotoMOB Extractor, has been developed to analyse the data from the text files and to allow the user to quickly and easily obtain the outputs mentioned in Figure 1 (C1, C2, C4, E1, E2, E3, E4, E5) in both AbN and GbN form. The actual and future version of the PhotoMOB toolbox as well as the PhotoMOB Extractor App are available with documentation at https://shiny.fannyville.com/PhotoMOB_Tool.html. The toolbox is currently only available for ArcGIS desktop, but will be soon converted to ArcGIS Pro and, additionally, our intention is to convert to the open source QGIS.

Acknowledgments

This research was undertaken under the MorphHab (PID2019104979RB-I00/AEI/10.13039/501100011033). It has also benefit from the research undertaken in the background of MorphPeak (CGL201678874-R/AEI/10.13039/501100011033) research projects funded by the Spanish State Research Agency (Ministry of Science and Innovation) and the European Regional Development Fund Scheme (FEDER). The first author has a grant funded by the Ministry of Economy, Industry and Competitiveness, Spain (BES-2017-081850). Damià Vericat is a Serra Húnter Fellow at the University of Lleida. All authors are part of the Fluvial Dynamics Research Group –RIUS, a consolidated group recognized by the Generalitat de Catalunya (2021 SGR 01114). We thank Alexandre Moron for building the square frame and the Pebble-Box device and his assistance, as well as Meritxell Puig and Estrella Carrero, for their assistance during the fieldwork campaigns and grains' measurement. Finally, we thank Jonathan Coutaz and Daniel Vázquez Tarrío for sharing training photos from the Buëch and Vénéon rivers.

CRediT authorship contribution statement

Fanny Ville: Conceptualization, Methodology, Investigation, Data curation, Formal analysis, Visualization, writing original draft, Writing – review & editing.

Damià Vericat: Funding acquisition, Methodology, Supervision Writing – review & editing.

Ramon J. Batalla: Funding acquisition, Methodology, Supervision, Writing – review & editing.

Colin Rennie: Methodology, Supervision, Writing – review & editing.

Data availability statement

Dataset of measured grain from field (from *paint-and-pick*), as well as manual grain digitalisation and automated grain delineation from *PhotoMOB* either *supervised* or *automated*, *Basegrain* and *Sedimetrics* are available under: https://zenodo.org/records/10038313

Declaration of competing interest

The authors declare that they have no conflict of interest.

References

Brenna, A., N. Surian, and L. Mao (2019). "Virtual Velocity Approach for Estimating Bed Material Transport in Gravel-Bed Rivers: Key Factors and Significance". In: *Water Resources Research* 55.2. Citation Key: Brenna2019a, pp. 1651-1674. DOI: 10.1029/2018WR023556.

Bunte, K. and S. R. Abt (2001). *Sampling Surface and Subsurface Particle-Size Distributions in Wadable Gravel- and Cobble-Bed Streams for Analyses in Sediment Transport , Hydraulics , and Streambed Monitoring*. Vol. 00. DOI: 10.1017/CBO9781107415324.004 PMID: 21939040. Ft. Collins, CO: U.S. Department of Agriculture, Forest Service, Rocky Mountain Research Station. DOI: 10.1017/CBO9781107415324.004. https://www.fs.usda.gov/treesearch/pubs/4580.

Bunte, K., K. W. Swingle, and S. R. Abt (2007). "Guidelines for using bedload traps in coarse-bedded mountain streams: Construction, installation, operation, and sample processing". In: *USDA For. Serv. - Gen. Tech. Rep. RMRS-GTR*, pp. 1-97. ISSN: 02775786.

Buscombe, D. (2008). "Estimation of grain-size distributions and associated parameters from digital images of sediment". In: *Sediment. Geol.* 210.1-2, pp. 1-10. ISSN: 00370738. DOI: 10.1016/j.sedgeo.2008.06.007. https://linkinghub.elsevier.com/retrieve/pii/S0037073808001279.

Buscombe, D. (2013). "Transferable wavelet method for grain-size distribution from images of sediment surfaces and thin sections, and other natural granular patterns". In: *Sedimentology* 60.7, pp. 1709-1732. ISSN: 00370746. DOI: 10.1111/sed.12049. https://onlinelibrary.wiley.com/doi/10.1111/sed.12049.

Butler, J. B., S. N. Lane, and J. H. Chandler (2001). "Automated extraction of grain-size data from gravel surfaces using digital image processing". In: *J. Hydraul. Res.* 39.5, pp. 519-529. ISSN: 00221686. DOI: 10.1080/00221686.2001.9628276.

Cassel, M., J. Lavé, A. Recking, et al. (2021). "Bedload Transport in Rivers, Size Matters but so Does Shape". In: *Scientific Reports* 11.1, p. 508. ISSN: 2045-2322. DOI: 10.1038/s41598-020-79930-7. (Visited on janv.. 16, 2023).

Cerney, D. L. (2010). "The Use of Repeat Photography in Contemporary Geomorphic Studies: An Evolving Approach to Understanding Landscape Change: Repeat Photography Use in Geomorphic Studies". In: *Geography Compass* 4.9, pp. 1339-1357. ISSN: 17498198. DOI: 10.1111/j.1749-8198.2010.00376.x. (Visited on mars. 16, 2023).

Chang, J. Cheng, J. Allaire, et al. (2023). *shiny: Web application framework for R*. Citation Key: shiny. https://CRAN.R-project.org/package=shiny.

Chang and C. Chung (2012). "Estimation of riverbed grain-size distribution using image-processing techniques". In: *J. Hydrol.* 440-441, pp. 102-112. ISSN: 00221694. DOI: 10.1016/j.jhydrol.2012.03.032. http://dx.doi.org/10.1016/j.jhydrol.2012.03.032%20https://linkinghub.elsevier.com/retrieve/pii/S0022169412002429.

Church and M. A. Hassan (1992). "Size and Distance of Travel of Unconstrained Clasts on a Streambed". In: *Water Resources Research* 28.1, pp. 299-303. ISSN: 19447973. DOI: 10.1029/91WR02523.

Church and M. A. Hassan (2002). "Mobility of bed material in Harris Creek: MOBILITY OF BED MATERIAL IN HARRIS CREEK". In: *Water Resources Research* 38.11. DOI: 10.1029/2001WR000753. http://doi.wiley.com/10.1029/2001WR000753.

Church, M. A. Hassan, and J. F. Wolcott (1998). "Stabilizing Self-Organized Structures in Gravel-Bed Stream Channels: Field and Experimental Observations". In: *Water Resources Research* 34.11, pp. 3169-3179. ISSN: 00431397. DOI: 10.1029/98WR00484. (Visited on mars. 16, 2023).

Church, D. McLean, and J. Wolcott (1987). "River bed gravels: Sampling and analysis". In: *Sediment Transport in Gravel-Bed Rivers* . Ed. by C. Thorne, J. C. Bathurst and R. D. Hey. John willey &

son. Citation Key: church1987. New York, NY, USA. Chap. 3, pp. 43-88. https://doi.org/10.1002/esp.3290140809.

Deal, E., J. G. Venditti, S. J. Benavides, et al. (2023). "Grain Shape Effects in Bed Load Sediment Transport". In: *Nature* 613.7943, pp. 298-302. ISSN: 0028-0836, 1476-4687. DOI: 10.1038/s41586-022-05564-6. (Visited on janv.. 16, 2023).

Detert, M. and V. Weitbrecht (2013). "User guide to gravelometric image analysis by BASEGRAIN". In: *Advances in river sediment research*. Ed. by S. Fukuoka, H. Nakagawa, T. Sumi and H. Zhang. Citation Key: Detert2013a ISBN: 978-1-315-85658-2 Pages: 165 Place: London Publication title: Advances in river sediment research Type: Other conference item tex.size: 8 p.. CRC Press, pp. 1789-1796. https://people.ee.ethz.ch/~basement/baseweb/download/tools/basegrain/ISRS2013_MDEWV_225.pdf.

Dietrich, W., J. Kirchner, H. Ikeda, et al. (1989). "Sediment Supply and the Development of the Coarse Surface Layer in Gravel-Bedded Rivers". In: *Nature* 340, pp. 215-217. ISSN: 0028-0836. DOI: 10.1038/340301a0.

Diplas, P. and J. B. Fripp (1992). "Properties of Various Sediment Sampling Procedures". In: *J. Hydraul. Eng.* 118.7, pp. 955-970. ISSN: 0733-9429. DOI: 10.1061/(asce)0733-9429(1992)118:7(955).

Folk, R. L. and W. C. Ward (1957). "Brazos River bar [Texas]; a study in the significance of grain size parameters". In: *J. Sediment. Res.* 27.1, pp. 3-26. ISSN: 1527-1404. DOI: 10.1306/74D70646-2B21-11D7-8648000102C1865D. https://pubs.geoscienceworld.org/jsedres/article/27/1/3-26/95232.

Graham, D. J., I. Reid, and S. P. Rice "Automated Sizing of Coarse-Grained Sediments: Image-Processing Procedures". In: *Mathematical Geology* 37.1. Citation Key: Graham2005a, pp. 1-28. DOI: 10.1007/s11004-005-8745-x. http://link.springer.com/10.1007/s11004-005-8745-x.

Graham, D. J., S. P. Rice, and I. Reid "A transferable method for the automated grain sizing of river gravels". In: *Water Resour. Res.* 41.7, pp. 1-12. ISSN: 00431397. DOI: 10.1029/2004WR003868. http://doi.wiley.com/10.1029/2004WR003868.

Graham, D. J., A. Rollet, H. Piégay, et al. (2010). "Maximizing the accuracy of image-based surface sediment sampling techniques". In: *Water Resour. Res.* 46.2, pp. 1-15. ISSN: 00431397. DOI: 10.1029/2008WR006940. http://doi.wiley.com/10.1029/2008WR006940.

Graham, D. J., A. Rollet, S. P. Rice, et al. (2012). "Conversions of Surface Grain-Size Samples Collected and Recorded Using Different Procedures". In: *J. Hydraul. Eng.* 138.10, pp. 839-849. ISSN: 0733-9429. DOI: 10.1061/(ASCE)HY.1943-7900.0000595. https://ascelibrary.org/doi/10.1061/%7B%25%7D28ASCE%7B%25%7D29HY.1943-7900.0000595.

Hassan, M. A. and P. Ergenzinger (2003). "Use of Tracers in Fluvial Geomorphology". In: *Tools Fluv. Geomorphol.* John Wiley & Sons, Ltd. Chap. 14, pp. 397-423. ISBN: 9780470868331. DOI: https://doi.org/10.1002/0470868333.ch14. https://onlinelibrary.wiley.com/doi/abs/10.1002/0470868333.ch14.

Ibbeken, H. and P. Denzer (1988). "Clast measurement: a simple manual device and its semiautomatic electronic equivalent". In: *J. Sediment. Res.* 58.4, pp. 751-752. ISSN: 1527-1404. DOI: 10.1306/212f8e36-2b24-11d7-8648000102c1865d.

Ibbeken, H. and R. Schleyer (1986). "Photo□sieving: A method for grain□size analysis of coarse□grained, unconsolidated bedding surfaces". In: *Earth Surf. Process. Landforms* 11.1, pp. 59-77. ISSN: 10969837. DOI: 10.1002/esp.3290110108.

Kellerhals, R. and D. I. Bray (1971). "Sampling Procedures for Coarse Fluvial Sediments". In: *J. Hydraul. Div.* 97.8, pp. 1165-1180. ISSN: 0044-796X. DOI: 10.1061/JYCEAJ.0003044. https://ascelibrary.org/doi/10.1061/JYCEAJ.0003044.

Mair, D., G. Witz, A. Do Prado, et al. "Automated finding, segmenting, and measuring of grains in images of fluvial sediments –the potential of transfer learning in deep neural networks". In: *Submitted to Earth Surf. Process. Landforms*. DOI: 10.31223/X51H31. DOI: 10.31223/X51H31. https://eartharxiv.org/repository/view/5523/.

Mao, L. (2012). "The Effect of Hydrographs on Bed Load Transport and Bed Sediment Spatial Arrangement". In: *Journal of Geophysical Research: Earth Surface* 117.3, pp. 1-16. ISSN: 21699011. DOI: 10.1029/2012JF002428.

Mao, L. (2018). "The Effects of Flood History on Sediment Transport in Gravel-Bed Rivers". In: *Geomorphology* 322, pp. 196-205. ISSN: 0169555X. DOI: 10.1016/j.geomorph.2018.08.046.

Mao, L., L. Picco, M. A. Lenzi, et al. (2017). "Bed Material Transport Estimate in Large Gravel-Bed Rivers Using the Virtual Velocity Approach". In: *Earth Surface Processes and Landforms* 42.4, pp. 595-611. ISSN: 10969837. DOI: 10.1002/esp.4000.

Ockelford (2011). "The Impact of Stress History on Non Cohesive Sediment Bed Stability and Structure". http://theses.gla.ac.uk/id/eprint/2577.

Ockelford and H. Haynes (2013). "The Impact of Stress History on Bed Structure". In: *Earth Surface Processes and Landforms* 38.7, pp. 717-727. ISSN: 01979337. DOI: 10.1002/esp.3348.

Ockelford, S. Woodcock, and H. Haynes (2019). "The Impact of Inter-Flood Duration on Non-Cohesive Sediment Bed Stability". In: *Earth Surface Processes and Landforms* 44.14, pp. 2861-2871. ISSN: 10969837. DOI: 10.1002/esp.4713.

Peckarsky, B. L., A. R. McIntosh, S. C. Horn, et al. (2014). "Characterizing Disturbance Regimes of Mountain Streams". In: *Freshwater Science* 33.3, pp. 716-730. ISSN: 2161-9549, 2161-9565. DOI: 10.1086/677215. (Visited on mars. 16, 2023).

Purinton, B. and B. Bookhagen (2019). "Introducing PebbleCounts: A grain-sizing tool for photo surveys of dynamic gravel-bed rivers". In: *Earth Surf. Dyn.* 7.3, pp. 859-877. ISSN: 2196632X. DOI: 10.5194/esurf-7-859-2019.

R Core Team (2020). *R: A Language and Environment for Statistical Computing*. R Foundation for Statistical Computing. Vienna, Austria. https://www.r-project.org/.

Sime, L. and R. Ferguson (2003). "Information on Grain Sizes in Gravel-Bed Rivers by Automated Image Analysis". In: *J. Sediment. Res.* 73.4, pp. 630-636. ISSN: 1527-1404. DOI: 10.1306/112102730630. arXiv: 03/073-630/$03.00 [1527-1404]. https://pubs.geoscienceworld.org/jsedres/article/73/4/630-636/99322.

Stähly, S., H. Friedrich, and M. Detert (2017). "Size Ratio of Fluvial Grains' Intermediate Axes Assessed by Image Processing and Square-Hole Sieving". In: *J. Hydraul. Eng.* 143.6, p. 06017005. ISSN: 0733-9429. DOI: 10.1061/(ASCE)HY.1943-7900.0001286. https://ascelibrary.org/doi/10.1061/%7B%25%7D28ASCE%7B%25%7D29HY.1943-7900.0001286.

Strom, K. B., R. D. Kuhns, and H. J. Lucas (2010). "Comparison of Automated Image-Based Grain Sizing to Standard Pebble-Count Methods". In: *Journal of Hydraulic Engineering* 136.8, pp. 461-473. DOI: 10.1061/(ASCE)HY.1943-7900.0000198. https://ascelibrary.org/doi/10.1061/%28ASCE%29HY.1943-7900.0000198%7D.

Team, R. C. (2022). *R: A language and environment for statistical computing*. Citation Key: R_stat. Vienna, Austria: R Foundation for Statistical Computing. https://www.R-project.org/.

Team, T. G. D. (2019). *GIMP*. https://www.gimp.org.

Vázquez-Tarrío, D. and R. J. Batalla (2019). "Assessing Controls on the Displacement of Tracers in Gravel-Bed Rivers". In: *Water* 11.8. Citation key: vasquez2019, p. 1598. DOI: 10.3390/w11081598. https://www.mdpi.com/2073-4441/11/8/1598.

Vericat, D., R. J. Batalla, and C. Garcia (2008). "Bed-material mobility in a large river below dams". In: *Geodinamica Acta* 21.1-2. Citation Key:vericat2008b, pp. 3-10. DOI: 10.3166/ga.21.3-10. https://www.tandfonline.com/doi/full/10.3166/ga.21.3-10.

Vericat, D., F. Ville, A. Palau-Ibars, et al. (2020). "Effects of Hydropeaking on Bed Mobility: Evidence from a Pyrenean River". In: *Water* 12.1, p. 178. ISSN: 2073-4441. DOI: 10.3390/w12010178.

Warrick, J. A., D. M. Rubin, P. Ruggiero, et al. (2009). "Cobble cam: Grain-size measurements of sand to boulder from digital photographs and autocorrelation analyses". In: *Earth Surf. Process. Landforms* 34.13, pp. 1811-1821. ISSN: 01979337. DOI: 10.1002/esp.1877. https://onlinelibrary.wiley.com/doi/10.1002/esp.1877.

Wolman, M. G. (1954). "A method of sampling coarse river-bed material". In: *Trans. Am. Geophys. Union* 35.6, p. 951. ISSN: 0002-8606. DOI: 10.1029/TR035i006p00951. https://doi.org/10.1029/TR035i006p00951%20http://doi.wiley.com/10.1029/TR035i006p00951.

Zingg, T. (1935). "Beitrag zur Schotteranalyse". Artwork Size: 102 S. Medium: application/pdf Pages: 102 S. DOI: 10.3929/ETHZ-A-000103455. http://hdl.handle.net/20.500.11850/135183.

S SUPPORTING INFORMATION

> **Note**
>
> Supporting Information for:
>
> **PhotoMOB: Automated GIS method for estimation of fractional grain dynamics in gravel bed rivers.**
> Part 1 : Grain size
>
> Contents of this file:
>
> This document provides supplementary material. It is structured using the same headings as the main article to help readers find what they are interested in reading more about. Title followed by the word "none" indicate that no supplementary information is provided for that section.

S.1 Introduction

To characterise and quantify mobilised sediment intensities, direct sediment sampling methods can be deployed (e.g., Helley and Smith, 1971 ; Bunte and Abt, 2001; Bunte et al., 2007) as well as indirect methods via for example the use of targeted tracer stones (e.g., Church and Hassan, 2002; Hassan and Ergenzinger, 2003 ; Vázquez-Tarrío and Batalla, 2019). The use of a painted plot is a commonly used indirect technique which involves painting a zone of the bed to use the coloured grains as a tracer. This method avoids alteration of the natural packing of the particles without limitation of the size of the traced grain. If entrained painted particles can be located downstream, then transport distances can also be measured (e.g., Church and Hassan, 1992; Hassan and Ergenzinger, 2003; Mao et al., 2017; Brenna et al., 2019; Vázquez-Tarrío and Batalla, 2019; Vericat et al., 2020).

However, the use of painted patches has several limitations (i) Firstly, the use of aerosols to ensure good paint adhesion may contaminate river surroundings. (ii) The paint must be applied to a dry substrate and allowed to dry before re-wetting. These conditions of use are not always available, as for example in rivers subject to hydropeaking, where water is released rapidly and large areas of the bed are frequently (daily, hourly) and quickly inundated. (iii) The measurements are focused on visually recovered downstream particles while the mobilised painted particles may deposit paint side down and/or be subsequently buried, resulting in a low recovery rate as reviewed by (Hassan and Roy, 2016). (iv) Finally, a large amount of information from the original patch location is not further analysed such as the proportion and size of immobile particles. A solution can be to compare successive images of the bed surface taken at the same location (Vericat et al., 2008; Cerney, 2010; Peckarsky et al., 2014). Information related to grain stability and mobility can be extracted by a spatial grain-by-grain inter-analysis of the particles present in the two photographs. In this case, a semi- or fully-automated image processing procedure is extremely useful. To meet this objective, we have developed an ArcGIS® toolbox to automate image processing in two distinct phases. The first part (this paper) consists of identifying and characterising all the grains present in the photos. This makes it possible to extract the size of the grains, their shape, their orientation and to estimate the proportion of the area covered by fine material. The second part (see companion paper Ville et al., 2023b) compares the shape of the grains positioned at the same coordinate between the photos in order to categorise them as immobile or mobile.

S.2 The PhotoMOB workflow

Figure **S**1 A represent the photo acquisition procedure while Figure **S**1 B represents the workflow of the *PhotoMOB* GIS toolbox Part 1.

S.2.1 Image collection

Once a target area has been selected, a frame with known exact internal dimensions is placed on the riverbed to physically delineate the area. The distance between each internal corner will be used to scale the images. In order to facilitate fieldwork and the subsequent scaling of the photos, a metal frame consisting of L-shaped side elements that are fixed together at their ends by a screw system can be used. The repetitive task of scaling the photos one after the other is facilitated by an area of interest of constant shape and surface, without any variation. The frame could include a measuring scale and a marker indicating upstream direction so that during office work the operator can quickly orientate the photo. The size of the area should be a function of the largest particle i.e., Diplas and Fripp (1992) proposed that the area to be sampled must be at least 100 times larger than the area of the largest particle. This would give an accuracy equivalent to a 100-grain Grid-by-Number sample, such as a pebble-count.

Finally, the photo is recommended to be taken facing against the flow direction, the more possible perpendicular to the riverbed, and with the area protected from direct sunlight to avoid brightness changes within the photo. In general, the more homogeneous the area is in terms of light and colours, the easier is to detect the particles automatically. Finally, the positions of the four corners of the frame can be marked and/or surveyed by a topographic method to enable to find back the location for a subsequent photo collection. Even if the precision of the method used to survey the corners of the frame is not the appropriate (i.e., cm) to scale the images, these coordinates will enable to return to the same location for subsequent photo collection. Once the area is re-visited, the frame is placed back on the bed, and the second photo is taken following the same protocol. This last field phase can be repeated for the same area successively according to successive flow events (as show in Figure **S**1 A).

S.2.2 Bed particle detection and characterisation

Grain detection and characterization is done in five steps represented in Figure **S**1 B. These five steps are grouped in two main processing tasks, which are fully described below. (i) Image pre-processing and (ii) image processing: (B.2) image classification, (B.3) image binarization, (B.4) boundary adjustment and (B.5) grain characterization.

S.2.2.1 Image pre-processing In order to facilitate good detection of the particles, the photos are first filtered externally to GIS in GIMP (Team, 2019), a free image manipulation software, to smooth the intra-grain noise while preserving edges. A high-pass filter is applied to the area inside the frame to sharpen the boundary of the particles which correspond to areas of rapid tonal change. It is a frequency filter that (i) preserves high frequencies via a first parameter named *standard deviation* that controls the level of detail preserved and (ii) increases them via the *contrast* parameter. This first filter depends strongly on the sunlight condition and the homogeneity of the surface. For fully painted photos with homogenous light (i.e., homogenized surface, low complexity) it is not necessary to use a high standard deviation value because the image contains few details (i.e., details correspond only to the particle edges) that are easily visible. For each photo in these conditions, a constant value of 5 for the *standard deviation* and 2.5 for the *contrast* paramete rare used. On the other hand, for unpainted photos or a variable lighting photo condition, is necessary to keep a higher level of detail in order to make the contours appear more clearly. A constant value of 10 for the *standard deviation* and 2.5 for *contrast* parameters are used. Then, for all conditions, a noise reduction filter with a constant *strength* of 10 is applied twice in succession, in order to attenuate the intra-grain noise. All these parameters were established by evaluating the performance of different values.

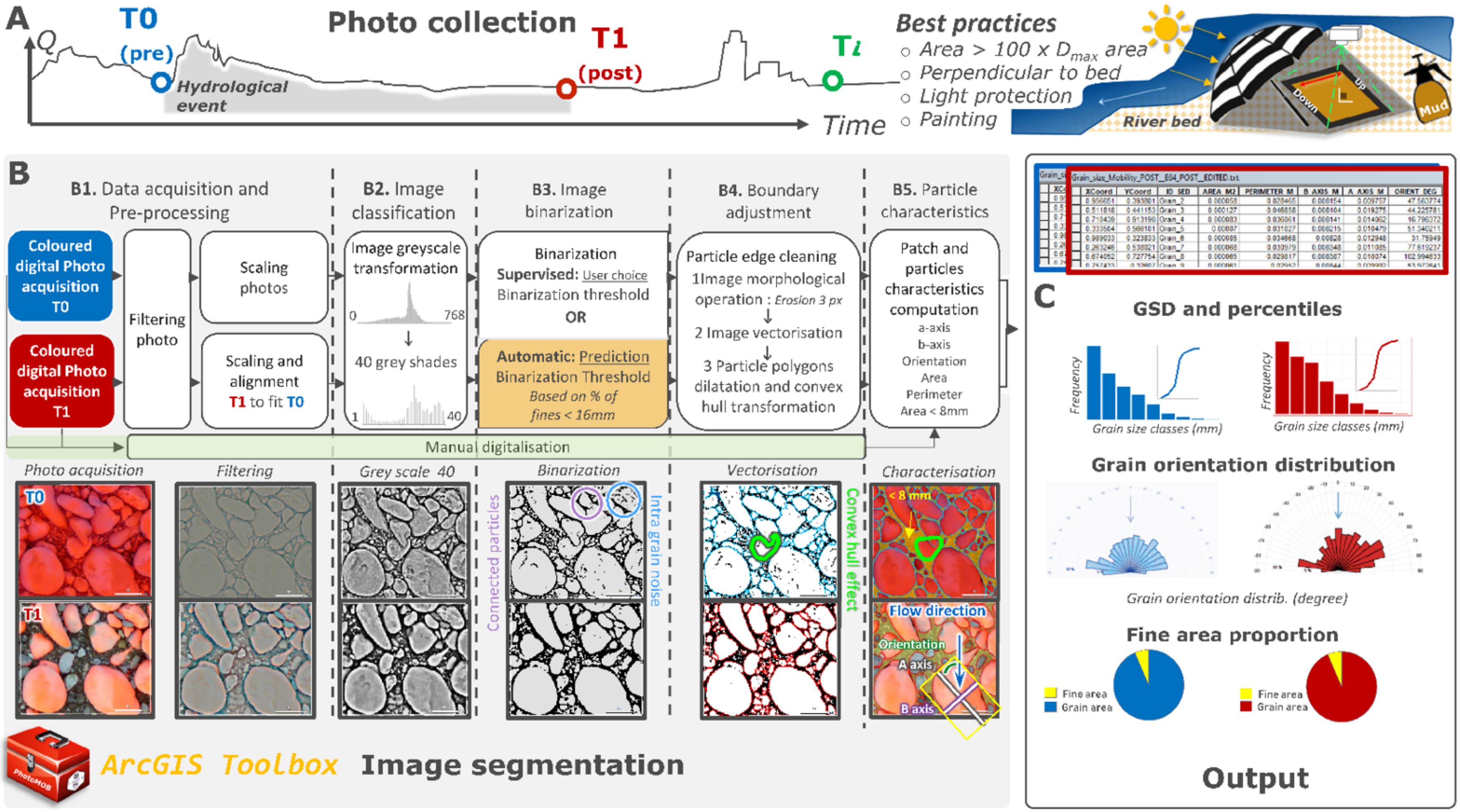

Figure **S**1: Illustration of the image segmentation workflow required to sample and characterise the bed surface. (A) Photo acquisition. (B) Extraction of grain and patch characteristics. (C) Possible output after patch surface characterisation. The yellow boxes represent the developed models of dark threshold prediction (see Text **S**2.2.3). Note the effect of the convex hull transformation on the green particle in the centre of the two images in the Vectorisation and Characterisation columns. In the Characterisation column, the second image shows the sketch explaining how particle characteristics are derived

Afterwards, the filtered images are loaded into GIS. The four internal corners of the frame are marked manually. They are used as Cartesian reference points on a local plan to scale the photo. For example, for a square frame with 1m sides (internal), points A, B, C and D receive the coordinates 0.1; 1.1; 0.0; 1.0 respectively. Then to correct the perspective of the image a projective transformation is applied. As it is difficult to get a perfect tilt free photographs without structure, this transformation removes the tilt and link the image to the ground for more accurate grain measurements.

In the case of partial or selective transport (i.e., when a certain proportion of the study area has remained stationary) the second or post event photo has to be aligned with the first one with a further projective transformation. This alignment is done manually by identifying identical points between the two photos. When all bed was disturbed and no reference points are found, the corner frame can be located at the same position of the first photo. In this case all grain will be new when compared to the precedent or first photo.

S.2.2.2 Image processing The scaled filtered images, are transformed into a grey scale image (intensity level) by simply summing the three bands (i.e., Red, Green and Blue). Each band can contain pixels with values ranging from 0 to 255. The grey scale image can thus finally present shades ranging from 0 (black) to 768 (white).

The next step is to transform these grey scale images into binary images, where the foreground would correspond to the particles (high intensity, white) and the background to the boundary of the particles and gaps (low intensity, black). To generate this binarization, a threshold of dark intensity must be selected to perform the partition. However, it is difficult to determine a threshold value out of 768 possibilities. Therefore, the grey scale levels are reduced (i.e., reclassified) from 768 to 40 levels *(ca. 5% of 768)*, and the threshold is identified from those 40 possibilities. This reduction allows the contour effect to appear (Tyagi, 2018). The selection of the threshold value relies on the use of the histogram of the frequency distribution of the grey levels of the pixels (method of moments corresponding of part B2 in Figure **S**1). The whole process can be *supervised* by the operator or be performed *automatically* through a threshold prediction model developed in this study and presented in Text S.2.2.3.

The boundaries of the particles in the binary images are not completely segmented. Sometimes there is still a chain-of-connection of some white pixels between two particles (shown in the Figure **S**1 B3). To remedy this, a morphological erosion operation is performed (Tyagi, 2018). This consists of increasing the black background area by a certain size and shrinking the white foreground area. It was established in this study, following multiple visual checks on different images, that an erosion of three pixels was optimal. Sime and Ferguson (2003) have also shown that a three pixel value allows for correct segmentation without amplifying too much the intra-grain noise. Then, the white pixel areas are converted from raster to polygons, vector features, yielding the outline of each particle (see Figure **S**1 B4). However, as these areas have been previously eroded, a dilation of the polygons is necessary in order to return to the original particle size. This dilation distance corresponds to three times the resolution of the raster (three times the pixel size of the image). Then, to smooth the rough contours of the particles and obtain a more realistic particle shape, a convex envelope is applied. This corresponds to an envelope passing uniquely through the extremities of the raw contour and eliminating any concavities. An example can be seen between the images in Figure **S**1 B4 and B5 (*Vectorisation* and *Characterisation*), which present the raw delimitation and the convex envelope (note the highlighted particle in the center).

Once this convex hull is generated, it is possible to extract six characteristics of the sediment patch. The (i) area and (ii) perimeter of each detected particle are directly acquired from the convex hull. For (iii) the longest axis (*a*-axis) and (iv) the intermediate axis (*b*-axis), on each particle, a minimum bounding rectangle box delimiting its smallest width is generated. The length of this rectangle corresponds to an estimate of the particle's *a*-axis, while its width corresponds to the particle's *b*-axis. Furthermore, the angle of the longest axis with north gives us information about (v) the orientation of the particle (see Figure **S**1 B5 and C). Finally, an estimate of the area covered by fin material is obtained by subtracting from the total study area, the summed area of particles with *b*-axis larger than fine limit defined by the operator (by default 8mm).

S.2.2.3 Training of a dark binarization threshold prediction model Butler et al. (2001) had already noted that this threshold depends on several factors such as (i) the sunlight condition, (ii) the scale of the photo, (iii) the source (camera), (iv) the texture (particle sizes). Since the photos are taken with the same camera under controlled light conditions and with fixed frame size, the most important factor for determining the optimal threshold is the general grain size of the study riverbed area. This phenomenon was captured by Sime and Ferguson (2003) using the term "image porosity". This term refers to the proportion of the image representing edges and gaps, which present low grey intensity levels (darker areas). The finer the grain size of the study area, the more edge pixels there are, and therefore the more number of black pixels there are in the image. Conversely, the coarser the grains, the fewer the number of pixels representing contours, and the fewer the number of black pixels. The method followed in this study is based on the intensity distribution histogram shape and statistical properties (Burger and Burge, 2016) (see Figure 2 *main text*). We assume that all photos, taken under the conditions described in the Figure **S**1 A and Text S.2.1, present a similar general shape of histogram, which is a skewed distribution toward the left side, i.e., toward low intensity (Figure 2 B *main text*). The binarization threshold for partitioning the image between particles (foreground) and interstices/boundary (background) will therefore be located towards the left of the histogram. Each image has a unique GSD and therefore a different proportion of interstice for the same study extent. It cannot be an absolute fixed value valid for all images. If the approximate proportion of pixels representing the background is known, then the binarization threshold could be set to this percentile. However, it appears difficult to give a visual estimation of the fraction of the image only occupied by the gaps and contours. Moreover, having only 40 grey levels, the percentile approach would be too sensitive. A bad estimate of ±15% would cause a change in the threshold value of ±6 levels. This would strongly change the delimitation.

Instead, we propose to develop a prediction model based on a visual approximation of the areal proportion of material finer than pebbles (<16 mm) covering the study area correlated with the optimal binarization threshold expressed not as a percentile but as a relative grey level value to a reference grey level value:

$$Reference\ grey\ level = mean\ value\ of\ the\ grey\ pixels\ levels - 1\ SD\ (\ grey\ pixels\ levels) \quad (\mathbf{S}1)$$

The prediction model was developed from a dataset of 68 surface river bed photos from five different rivers [Cinca (Spain) , Ésera (Spain) , Vénéon (France), Buëch (France) and Blanco-Este (Chili)] covering areas from 0.16 to 1 m². Since it was not always possible to paint the area or to protect it from direct sunlight, we have created a training dataset divided into three groups corresponding to different photo conditions (see Figure 2 D *main text*). Condition C1, corresponds to painted areas protected from the sun (optimal condition). Condition C2 corresponds to unpainted areas but still protected from the sun (degraded condition). Finally, condition C3, corresponding to unpainted areas and not protected from the sun (inadvisable condition). The photos were scaled and digitized by hand (Figure 2 A *main text*). This is the *gold standard* i.e., the best delineation that can be expected. In total, 34246 particles were delineated manually. These delineation layers were fed into the tool to perform step B5 on Figure **S**1 (Particle characterization). The *b*-axis size of each particle could be calculated. All areas of the image covered by polygons representing particles with a *b*-axis greater than 16 mm were subtracted from the study area; this allows us to know the area covered by finer materials than pebbles.

In parallel, each of the same images was processed in the tool. For each of them, 22 grey levels were tested as a threshold for binarization. In total, 1496 delineation proposals were generated (68 photos × 22 tested thresholds). The 22 binarization thresholds tested are expressed as a relative value to the reference value as illustrated in Figure 2 B (*main text*) and Equation **S**1. Then, from these 22 delineations, a single operator selected the best delineation. In order to remain consistent on the comparison of all these particle layers, for each photo, the delineations were compared two by two, from the lowest threshold level (*Reference value - 5*) to the highest (*Reference value + 16*), preferring to keep a layer with a few under-delineations rather than a layer with a large number of over-delineations for two main reasons: (i) because if a manual edge correction (edition) is desired, a few polygons to segment is a faster operation than removing a large number of small polygons and then re-delineating them correctly; and, (ii) furthermore, by using the Area-by-Number form to establish the particle size distribution, each particle present has the same representativeness in the sample. Adding a large number of false small particles will have more impact on the final result than keeping a few large false particles.

The result of all these steps is (i) the proportion of the photo covered by material smaller than 16 mm and (ii) the optimal binarization threshold. Figure 2 C (*main text*) shows the prediction models of the binarization threshold established via these pairs of information, specific to each photo condition (C1, C2, C3). The R-square of 0.74 (p-value <0.001) for the C3 predicting model is lower than the ones for C1 and C2 respectively 0.85 (p-value <0.001) and 0.89 (p-value <0.001). In condition C3 the optimal threshold is less conditioned by the GSD than by the variation in image brightness. To obtain an order of magnitude of the error of these prediction models, a validation set of 11 patches photographed in the three conditions with proportions of area below 16 mm ranging from 15% to 71% was collected. The mean absolute error of prediction is 1 grey levels for photo condition C1 and C2, whereas in C3 it is of 2 (average distance between the model line and the validation point for each photo condition on Figure 2C, *main text*).

S.3 Method of performances and compatibility assessment

None

S.3.1 Control dataset

S.3.1.1 Control data set acquisition The data set consists of 10 patches, seven from Cinca river and three from Ésera river. Each of the 10 patches was photographed in 3 different conditions (see Figure **S**2 part A below). Once the patches had been painted and the last photo taken, all the whole grains inside the frame were collected and their position on the bed estimated and classified into three categories based on the projection of the paint on their surface (Figure 3 *main text*). This position can be compared to the work of Ibbeken and Schleyer (1986) , see Figure **S**2, part B below.

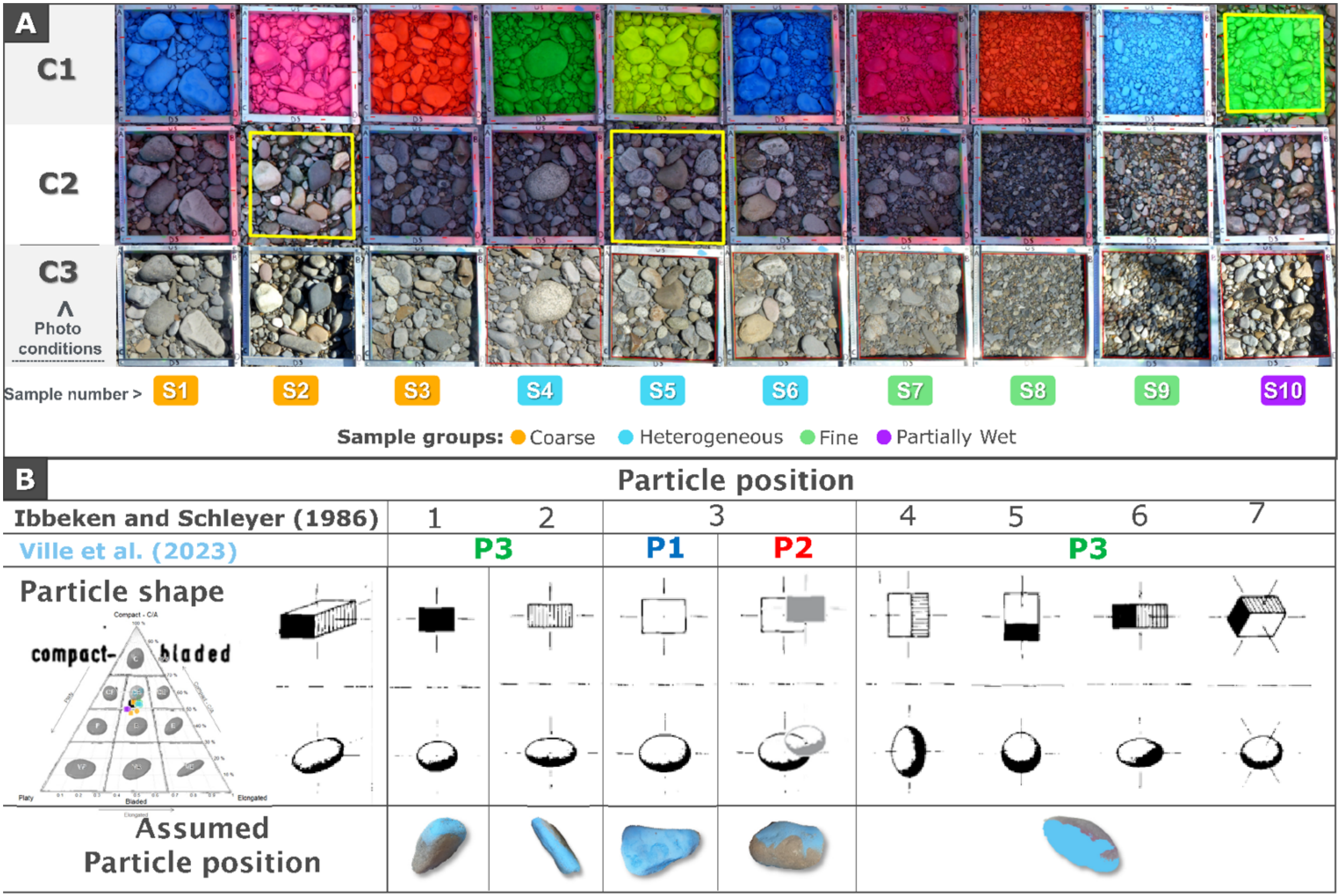

Figure S2: (A) Illustration of the 10 40*40 cm samples for the 3 photo conditions. C1: painted and protected from the sun, C2: unpainted but protected from the sun and C3: unpainted and unprotected from the sun. Samples were divided into three groups according to grain size and lithology. (B) Classification of grain position (indicative of degree of imbrication) based on the work of Ibbeken and Schleyer (1986) (modified after Ibbeken and Schleyer (1986)).

S.3.1.2 Control data set characteristics According to the Zingg classification Figure **S**3 A the median shape of the sampled particles from both rivers is spherical. However, the lithology and shape of all these particles varies between rivers i.e., the sediments of the Cinca consist mainly of coarse-grained white granite (increasing the complexity of the photographed surface to be segmented) and pale limestone. The seven samples from this river as well as sample S9 (from Ésera River) are composed approximately of 50% spherical particles, then 30% discoidal particles (quite flat), and about 10% bladed and rod-like particles (elongated) (Figure **S**3 B and C). The Ésera sediments are dominated by dark sandstone with varying degrees of metamorphism. The particle shapes of the two coarse samples S2 and S10 from this river are significantly different from the other seven with predominantly discoidal shapes (41 and 49% respectively), followed by spherical shapes at 30%.

Samples 1 through 3 were grouped as having a coarse particle size distribution (D_{50} in GbN form ranging between 44 mm to 57 mm). Samples S1 and S2 were dominated at 38% and 37% by particles in the P1 position (fully visible) while S3 is the only sample dominated by particles in the P3 position (39%). Samples 4 through 6 were dominated by articles in P2 position (i.e., overlapped, between 39% and 45%), all from the Cinca, and were grouped as having heterogeneous surfaces. Samples 4 and 5 were heterogeneous in terms of lithology, while sample 6 has a low grain sorting coefficient (Folk and Ward, 1957) of 1.3 (poorly sorted). Samples 7 through 9 were representative of fine patches composed of between 38 and 71% material finer than pebbles (16 mm) and with D_{50} in GbN form between 14 to 22 mm. S7 has similar proportions of particle in P1 and P2 (around 35%), while samples S8 and S9 are largely dominated by particle in P1 position (fully visible) at 48 and 49%. Finally, the last sample S10, was collected because it had a partially wet surface. As 49% of the sample is disc-shaped (flat and circular) and dominated at 38% by particle in position P2, it will be difficult to characterise correctly by photographic methods.

In spite of notable differences in size and shape between rivers and groups of samples, all samples show a similar evolution of the median shape with increasing size (*b*-axis) visible in Figure **S**3 B. This can be broken down into 3 phases: (i) First, between 5.66 and 11 mm there is a significate progressive decrease in elongation and an increase in sphericity (p-value < 0.5) while the flatness remains stable. The p-values of the statistical Mann-Whitney tests between size classes are given in Figure **S**3 D. (ii) Secondly, between 11 and 45 mm, the median shape of the particles becomes progressively more elongated and flatter towards a bladed shape. (iii) Finally, there is an abrupt change in trend for the particles above 45 mm, when they become more compact with a discoidal tendency.

In addition, all the samples are composed of particles of similar shape in P1 and P2, while all of them present particles in P3 with a significantly more spherical shape (less elongated and less flat). The proportion of P3 particles (necessarily under-estimated by photographic method) varies between 12 and 40% within the 10 samples. In a study comparing the photographic method with the more traditional pebble-count method, Strom et al. (2010) observed at six different sites with little or no particle imbrication, a proportion of P3 particles varied between 10 and 22%. The proportion of P3 in our study appears to be consistent, although some of our samples show lot of imbrications.

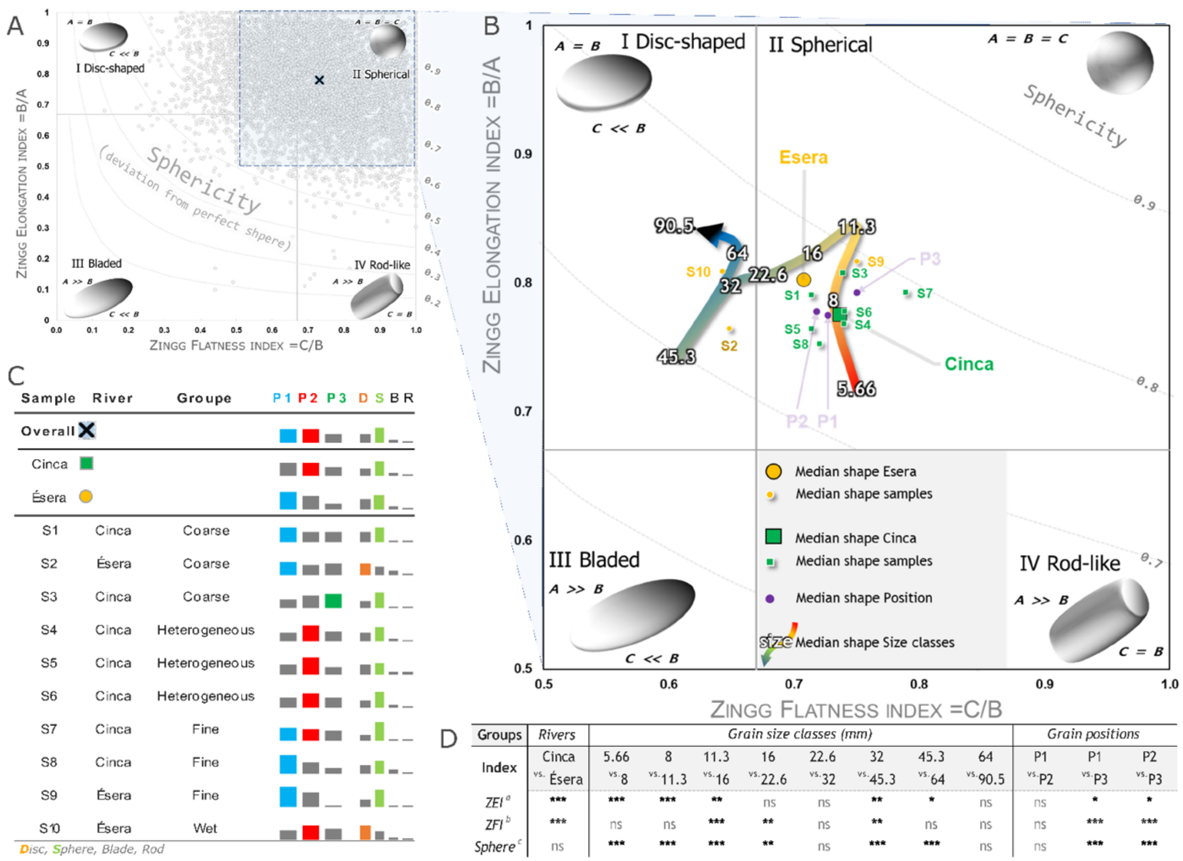

Groups	Rivers	Grain size classes (mm)								Grain positions		
Index	Cinca vs. Ésera	5.66 vs. 8	8 vs. 11.3	11.3 vs. 16	16 vs. 22.6	22.6 vs. 32	32 vs. 45.3	45.3 vs. 64	64 vs. 90.5	P1 vs. P2	P1 vs. P3	P2 vs. P3
ZEI [a]	***	***	***	**	ns	ns	**	*	ns	ns	*	*
ZFI [b]	***	ns	ns	***	**	ns	**	ns	ns	ns	***	***
Sphere [c]	ns	***	***	***	**	ns	***	***	ns	ns	***	***

Figure **S**3: Characteristic of control particles. (A) Classification of the shape of each particle according to the classification of Zingg (1935) and the overall median shape. (B) Median Zingg flatness and elongation index by (i) rivers (Esera in yellow circle and Cinca in green square), (ii) samples (S1-S10), (iii) size classes (warm to cold colour gradient) and (iv) position on the bed (purple circle). (C) Proportion and dominant (coloured bar) proportion of particle position and shape by groups (D) Mann-Whitney test of statistical significance of the shape disparity between the rivers, consecutive grain size classes and positions of the bed particles: * significant test on α=0.05, ** significant test on α=0.01, *** significant test at all levels, ns: insignificant test, [a] Zingg Elongation Index (*b/a*), [b]Zingg Flatness Index (*c/b*), [c]Krumbein shpericity index: $[((b*c)/a^2)(1/3)]$ (Krumbein, 1941)

S.3.2 PhotoMOB assessment

S.3.2.1 Assembling of the dataset Figure 4 (*main text*) presents an overview of the digitization results obtained in a *supervised* manner (i.e., using the segmentation tool but with the binarization threshold selected by the operator) in the three photographic conditions (columns) for a sample from each group (rows). The particles at the edge are removed from the analysis due to the metallic frame visible in the photographs. Only the particles entirely within the frame were retained for the purpose of this performance analysis to allow a comparison with the *paint-and-pick* on the same exact grain population.

In condition C1, the samples show some under-segmented particles (labelled U in Figure 4 first column), mainly concerning large overlapped particles. The contrast is not strong enough to separate them well. In addition, some particles are left out of the count (labelled U_e) because they are under-segmented (i.e., joined to other particles) and bounded by a polygon touching the edges. The under-segmentation is due to the pixel foreground still being connected despite the morphological erosion operation in step B4 Boundary adjustment.

In C2 condition there is generally a little more under-segmentation (Figure 4, second column); this time it concerns to the wider range of grains. This will result in the loss of some intermediate grains and the detection of some very large *non-real* particles. The two heterogeneous samples S4 and S10 show more anomalies (Figure 4, second column, 3rd and 4th row). In S4 the large center particle is very over segmented because of its mineralogy whereas in S10 a large number of particles are grouped to form large false particles. The wet areas, such as the area labelled U in the upper left or the two Ue on the right, are not well segmented because they are formed by a set of pixels that are darker than the rest of the image forming relatively lighter areas that are dry. Such a partially wet condition causes the same problem as in condition C3.

In C3 (Figure 4, last column), the delineation process is less efficient; many particles are under-segmented and a large part of the image is discarded. Further, for the heterogeneous sample S4 there is more over-segmentation of the large central granitic particle than in C2.

S.3.2.2 GSD computation and percentiles extraction

S.3.2.2.1 Continuous measurement or real measure of grains The extraction of percentiles in the form of Area-by-Number and Grid-by-Number for the image-based GSD and for the control data measured with the Pebble-Box (all giving *continuous* measurement axis) was carried out following the principles explained by Bunte and Abt (2001) and Graham et al. (2012) as follows:

1. In each data table representing a sample where each line represents the attributes of a given detected grain, a *b axis* column indicating the *b*-axis value and an *Area* column indicating the area of each particle were used. For the distribution from the Pebble-Box, the surface area of the particles was estimated by calculating the area of an ellipse by knowing the *a* and *b* axis (Area = *(a/2)* * *(b/2)* * pi). Within each sample, *b*-axis grains smaller than 8 mm have been excluded.
2. It can sometimes happen that some grains have exactly the same size, especially in the control data from the Pebble-Box. The grains were grouped by identical *b*-axis size value.
3. A column *Nb* was added to calculate the number of grains for each single *b*-axis size value. An example of such a table is shown in Figure **S**4 A1 for sample S4.
4. A *Total area* column has also been added (Figure **S**4 A2) to calculate the sum of the surface area occupied by the grains of strictly identical size.
5. The table was sorted in ascending order from column *b axis*.
6. A *Frequency* column was created to calculate the frequency of occurrence (Nb) of each unique grain size within the sample.

A

A1 — Truncation 8mm — A2

A1 Area by Number: *b* axis (mm)	Nb	Freq. (%)	Cumulative Freq. (%)	A2 Grid by Number: *b* axis mm	Total Area (mm²)	Freq. Area (%)	Cumulative Freq. Area (%)
8.0	10	2.8	0.0	8.0	724	0.4	0.0
8.1	1	0.3	2.8	8.1	70.6	0.0	0.4
8.2	5	1.4	3.1	8.2	349	0.2	0.4
	...				...		
11.5	15	4.2	40.1	38.5	2009	1.1	46.4
11.7	1	0.3	44.4	39.5	127	1.0	47.5
12.0	13	3.7	44.6	40.0	2026	1.1	48.5
12.5	13	3.7	48.3	**40.5**	2228	1.1	49.6
13.0	6	1.7	D_{50} 52.0	**44.0**	872	1.1	D_{50} 50.7
13.5	6	1.7	53.7	45.5	1044	1.2	51.8
14.0	7	2.0	55.4	48.5	1280	3.0	53.0
	...				...		
64.0	1	0.3	98.6	64.0	4523	2.4	77.7
66.0	2	0.6	98.9	66.0	8086	4.4	80.1
70.5	1	0.3	99.4	70.5	5426	2.9	D_{84} 84.5
156.0	1	0.3	99.7	156.0	23401	12.6	D_{90} 87.4
156.001	0	0.0	100.0	156.001	0	0.0	D_{95} 100.0

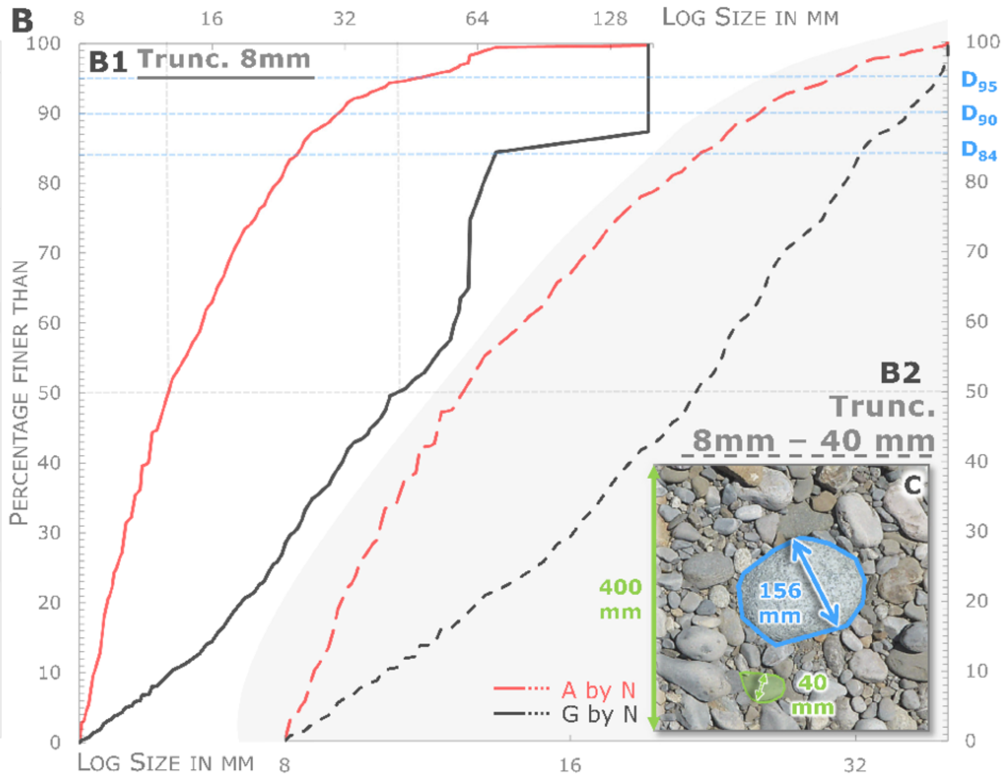

Figure **S**4: (A) Illustration of the procedure for extracting cumulative particle size distributions and percentiles, with the example of the sample S4 in (A1) AbN and (A2) GbN. (B) Grain size distribution of sample 4. (B1) Distribution in the form of Area-by-Number (in solid red) and Grid-by-Number (in solid black) with low truncation at 8mm. Note the problematic shape of the end of the Grid by Number distribution. (B2) Distribution in the form of Area-by-Number (in dashed red) and Grid-by-Number (in dashed black) with a low truncation at 8mm and a high truncation at 40 mm. The value of 40 mm corresponds to the value of the theoretical maximum sampleable diameter for this 400 mm long square. (C) Illustration of sample S4.

7. Finally, a *Cumulative Frequency* column was created to calculate the percentage of grains in the sample below each unique size detected. In order to follow the method described in Bunte and Abt (2001), for the extraction of percentiles, this column accumulates the values of the Frequency column with a lag of 1 so that 0% of the distribution is below the value of the finest particle encountered. It was therefore necessary to add a last row at the bottom of the table to arrive at a total accumulation of 100%. In this last row, we have indicated in the column *b axis,* the maximum size encountered +0.001 mm. In the case of the Area-by-Number analysis, this does not lead to any problems. Despite the small number of relatively large particles, the penultimate row of the cumulative frequency column always contains values above 99%. This does not lead to any errors in the analysis of the comparison of the different Area-by-Number particle size distributions depending on the acquisition procedure.

To estimate the distribution in Grid-by-Number form:

8. A *Frequency Area* column was created, where the percentage of area represented by each grain size was calculated.
9. In a column *Cumulative Frequency Area* the cumulative sum of the column *Frequency Area* was calculated. Here too, a shift of one row was made.
10. For both forms of distribution, the percentiles were obtained by interpolation only between two grain sizes located on either side of the desired percentile.

It should be noted that the estimation of percentiles in Grid-by-Number (GbN) form (solid left black curve) compare to Area-by-Number (AbN) form (solid red left curve) (Figure **S**4 B1) can be subject to errors if the criterion proposed by Diplas and Fripp (1992) is not met, because the relative weight of the particles in the distribution is proportional to their surface area. As in the example in Figure **S**4 B1 and C, a single large particle impacts the end of the GbN GSD (left solid black curve) and thus the estimation of the largest percentiles (here probably from the D_{75} but strongly visible from the D_{84} onwards). Figure **S**4 B2 illustrates the shape of the cumulative GSD for the same sample in AbN (right dashed red curve) and GbN (right dashed black curve) but with this time a high truncation at 40 mm allowing to respect the criterion of Diplas and Fripp (1992) by excluding the largest particles too few to be correctly characterized. The value of 40 mm corresponds to the value of the theoretical maximum *sampleable* diameter for this 400 mm long square. A detailed evaluation of the effect of expressing the GSD from the photos as GbN form and the importance of respecting a minimum sampled area based on the largest clast is presented in 4.2.1 of the *main text*.

S.3.2.2.2 Discrete measurements or binned b-axis sizes

None

S.3.2.3 Performance and compatibility assessment

None

S.4 Results and discussion

S.4.1 Performances

S.4.1.1 Grain's detection - Comparison to manual grain distribution or Gold standard

None

S.4.1.1.1 Condition 1 – Painted and Sunlight protected

None

S.4.1.1.2 Condition 2 – Not Painted but Sunlight protected

None

S.4.1.1.3 Condition 3 – Not Painted and Not Sunlight protected

None

S.4.1.2 Photographic method performance - Comparison to real bed distribution or Paint-and-pick

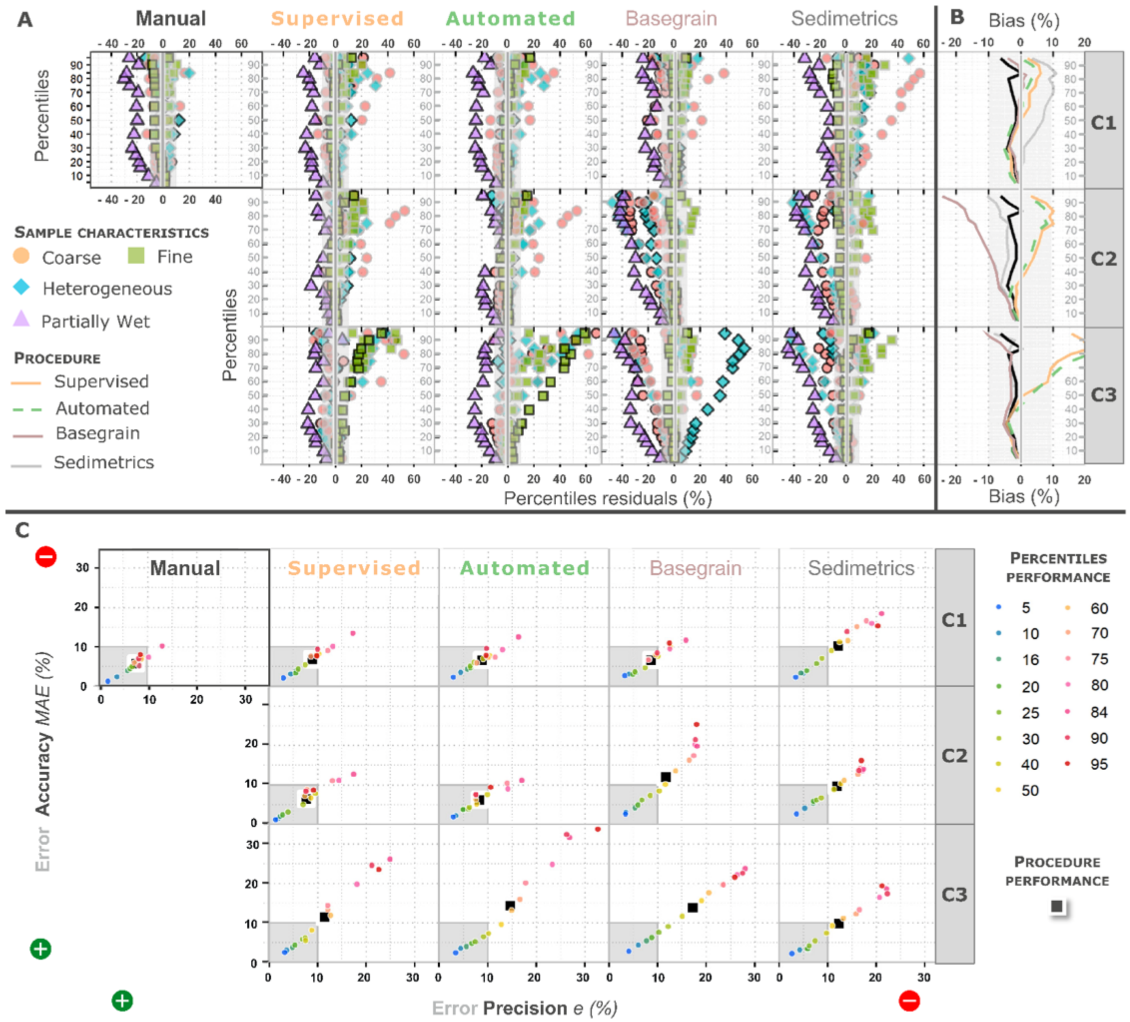

Figure **S**5: Performance assessment of image processing procedures compared to *pain-and-pick* bed surface sampling. (A) Distribution of the 150 relative residuals of percentiles estimation (15 percentiles * 10 samples) under the three photo conditions for the manual, *supervised* and *automated PhotoMOB* procedure as well as for *Basegrain* free stand-alone tool from Detert and Weitbrecht (2013) and *Sedimetrics Digital Gravelometer*™ from Graham (2005a, 2005b). Manual digitalisation was performed only on painted photos (C1). The residuals are coloured according to the 4 main patch characteristics (coarse, fine, heterogeneous, partially wet). Samples taken as example in Figure 4 (*main text*) are represented here by symbols with black outlines. (B) Relative bias of percentiles estimation for each procedure. Bias is calculated over residuals of the 10 samples. (C) Average relative performance (accuracy and precision) for the estimation of each percentile (coloured dots), as well as the overall performance (black square) of the 5 procedures. The vertical shaded areas mark the 10% error limits.

S.4.1.2.1 Manual delineation None

S.4.1.2.2 Automated delineation None

S.4.1.3 Limitations and further developments

S.4.1.3.1 Limitations None

S.4.1.3.2 Methodological improvements for image acquisition and processing Figure S6 shows photos example without (C2) and with the clay solution (C1 clay) on a sample with a large number of particles that can cause over-segmentation (coarse mineral, veined...). The automated digitization obtained by *PhotoMOB* on the photo painted with our solution (C1 clay) shows almost no over-segmentation compare to C2 (Figure S6 - B, top and bottom images in *PhotoMOB* column). The graph on the bottom (Figure S6 - C) shows the positive impact of adding the clay solution. In case of C2 (solid red curve), despite the number of grains detected (1327) being very close to the manual procedure (1388), there is an under-estimation of the entire GSD due to an over-segmentation of the grains as can be seen in Figure S6 - B. The C1 Clay painted automated delimitation (red dashed curve) is closer to the manual delineation (black curve) except for the coarse grain sizes where D_{95} is over-estimated due to the under-segmentation (union) of some grains. However, the error in estimating the D_{50} was reduced from -12.2% to -3%. Therefore, the use of a clay solution allows a homogenization of the photographed scene. There is a reduction of the complexity of the image, the only details (dark pixel) correspond to the edge of the grain (almost no detail intra grain left). Moreover, the clay reduces the reflectance of the surface by its colour and matte texture which absorbs the light instead of re-emitting it and this even better than the spray paint. The use of this solution and the performance of our procedure in C1 are very encouraging. Good quality delineations will require little time and effort for correction by the operator to proceed to the next stage of mobility characterisation. We also tested the new software developed by Mair et al. (Preprint EarthArXiv 2023). This new procedure makes it possible to obtain very correct delineation in condition C2 and also in C3 (C3 not shown in this image for lack of space). We also tested it on fluorescent spray-painted images (condition C1). Unfortunately, the algorithm was not trained on painted sediment (C1). However, these results are very encouraging, and in the near future it may be possible to train their procedure with our manually digitised data on photos painted or partially painted. This will greatly reduce the boundary correction effort.

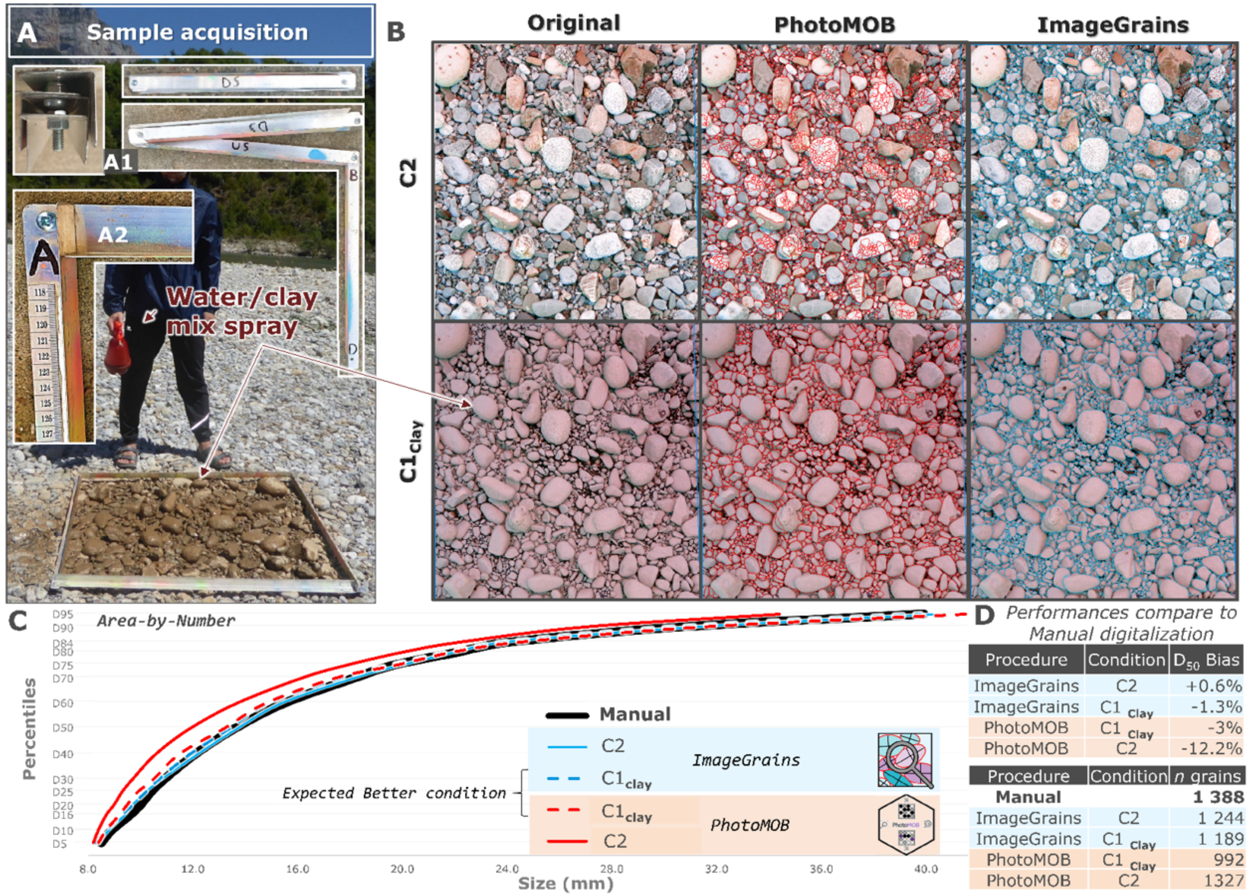

Procedure	Condition	D_{50} Bias
ImageGrains	C2	+0.6%
ImageGrains	C1 clay	-1.3%
PhotoMOB	C1 clay	-3%
PhotoMOB	C2	-12.2%

Procedure	Condition	*n* grains
Manual		**1 388**
ImageGrains	C2	1 244
ImageGrains	C1 clay	1 189
PhotoMOB	C1 clay	992
PhotoMOB	C2	1327

Figure **S**6: Illustration of solution for a better grain segmentation (A) Application of the clay/water solution to the study area. (B) Example of grain segmentations in the study area for both conditions C2 (top) and C1 with clay paint (bottom). Left, original images and, middle and right, *PhotoMOB* and *ImageGrains* (Mair et al. (Preprint EarthArXiv 2023)) segmentation results. (C) Percentiles from manual digitalization (black curve) compared to automated procedures in C2 condition (solid curves) and in C1 Clay painted condition (dashed curve). (D) Performance for D_{50} estimation and grain number estimation. Finally, in (A2), note the L-shape of the metal frame elements fixed together at their ends by a screw system (A1). This allows the frame to be folded on itself to not be cumbersome and to have a strict square shape that is always identical between each photo thanks to the stop in the corners formed by the L shape. The repetitive task of scaling the photos one after the other is facilitated by an area of interest of constant shape and surface, without any variation.

S.4.2 Compatibility with existing GbN data

S.4.2.1 GbN performances

None

S.4.2.2 Compatibility between continuous and discrete square holes measurements For sample S2 (dominated by coarse and discoid (flat) particles) and S9 (fine and spherical particles), each particle, before being measured in the Pebble-Box, was passed through a template with several sieve-sized square-holes *D* with 0.5 psi -increment (psi = log2(b)) to replicate a sieving machine. The median shape of the samples is visible in Figure **S**3 B. The *D/b,* of both samples, per grain size classes is presented in Figure **S**7, below. Particles smaller and coarser than 16 mm (pebble limits) have different flattening index, resulting in markedly different *D/b* ratios.

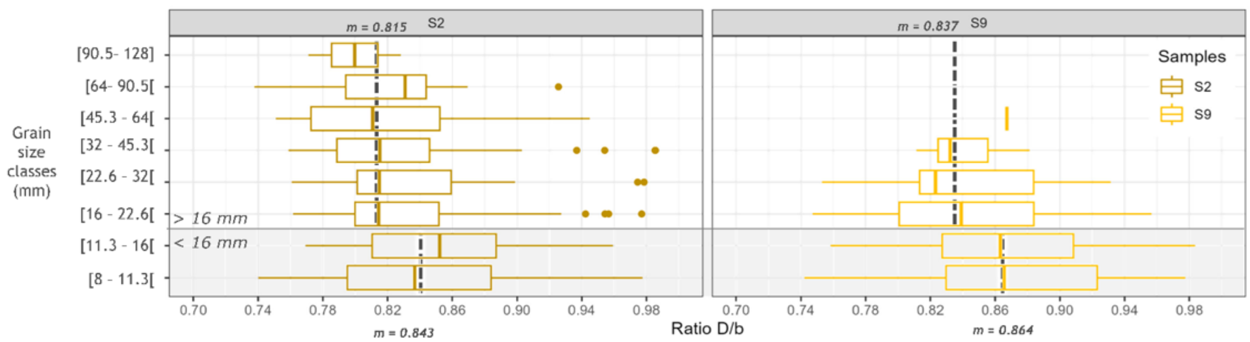

Figure **S**7: Dispersion of *D/b* ratio per grain size classes for the 2 sample (S2 and S9) with *b*-axis measured with the template and Pebble-Box. Black dashed vertical lines indicate median *D/b* ratio per particle < and > to 16 mm.

Finally, Figure **S**8 shows the impact of compliance with the Diplas criterion and the axis measurement method for the manual and *supervised PhotoMOB* procedures. This figure illustrates the important points to consider when using the data from the photographic method, summarized in 4.2.3 of the main text, by following the arrows of the boxes in the legend. On the first (part A) column are the RMSE for percentiles estimates for the manual (top) and *supervised PhotoMOB* procedure (bottom) for C1 condition. The condition for the one *PhotoMOB* was developed. It shows the deviation from the real control set measured with *continuous* data (Pebble-Box). Solid line represent the GSD of all the grain >=8mm in AbN (red) and GbN (black) while the dashed line represent the errors with truncated GSD at 40 mm to meet the Diplas criteria. The gain of performance is visible. Dashed line (red (2) and black (6)) are below 10% RMSE. AbN error are reduced by one third while GbN by half. The top and bottom plot are quite similar reflecting the good performance of *PhotoMOB* to reproduce the gold standard behaviour.

The second column (B) is the deviation from the real control set but measured with *discrete* data (square holes' template). This only concerns the two samples S2 and S9. Again, solid red and black line represent the GSD from all the apparent grain on the image with the manual (top) and *supervised* procedure (bottom). In GbN we can observe large error for estimates of high percentiles. With the truncation at 40mm (dashed black lines), the error stayed below 20%. Problem of under-segmentation take lot of importance in GbN specially when they are small in term of number and area sampled not adequate.

Then the red solid (1) and red dashed (2), high truncation, are overlapped showing no strong impact of sampling a too small area in AbN. In green (7) is represented the AbN GSD truncated to meet the Diplas criteria and converted to sieve data (via Church equation and by average flatness ratio). The green dashed line is localized close to the red solid and dashed lined.

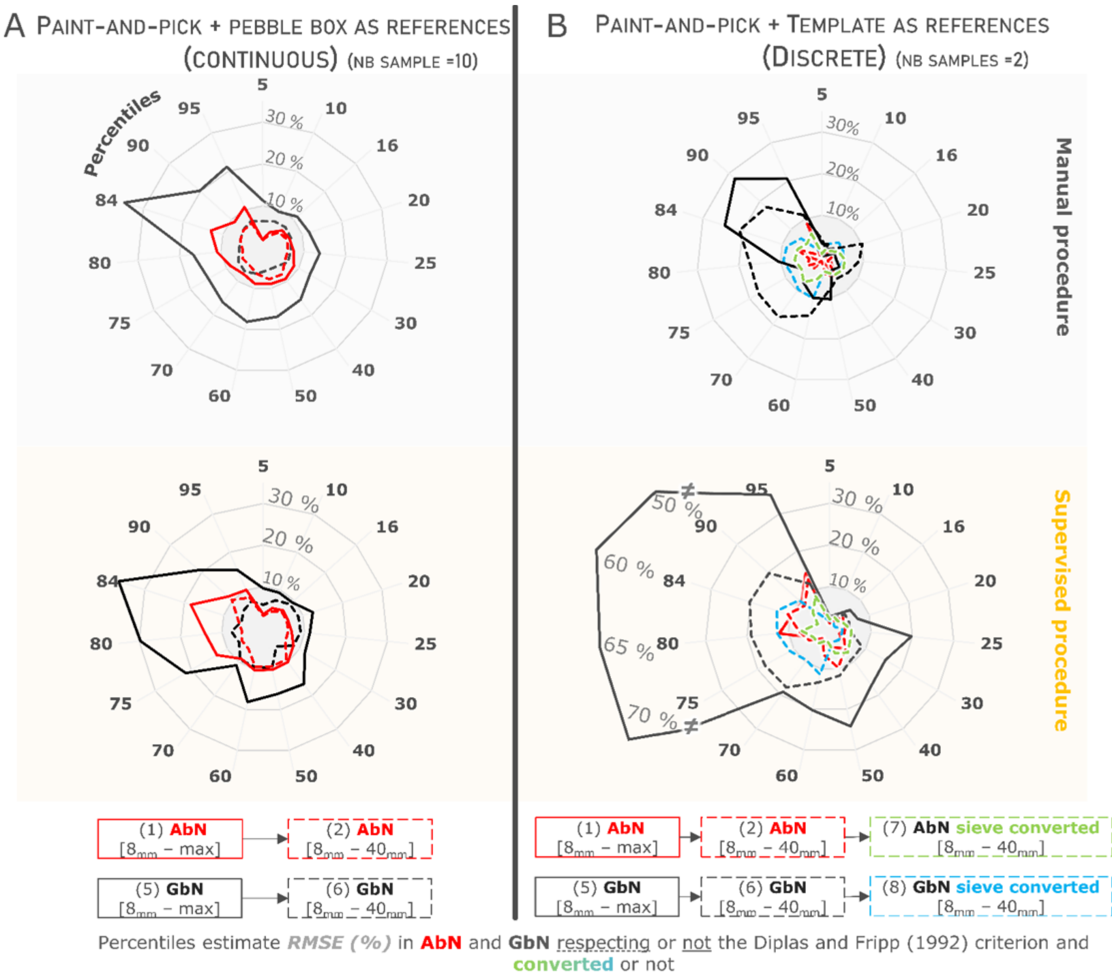

Figure **S**8: RMSE for the estimation of the 15 percentiles analysed in relation to the grain actually present in the bed. Top for manual procedure, bottom for *supervised PhotoMOB* procedure. (A) Data from photos (manuel or *supervised*) are compared with *paint-and-pick* grains measured with the Pebble-Box. (B) Data from photos are compared with *paint-and-pick* grains measured by the template. The numbers in brackets in the legend refer to the mean RMSE presented in Figure 7 of the *main text*. Solid curve represent the percentile from GSD with only low truncation at 8mm for AbN (red (1)) and GbN (black (5)) while dashed line represent GSD with low and high truncation (8mm to 40mm) to meet the Diplas criterion (2 and 6). Finally, the truncated and converted distribution according to average flatness of Cinca and Ésera river (7) and (8). The shaded areas mark the 10% error limits.

Under estimation of percentile from photos because of fabric effect is of the same amount than the measure bias of the sieving method. This make directly comparable AbN size from the photo with size from template.

In blue (8) is represented the GbN GSD truncated to meet the Diplas criteria and converted to sieve data (via Church equation and my average flatness ratio). The blue dashed line in localised below or close to 10%. This indicate that in GbN, converting the *b*-axis size reduce by half the deviation between size measurement from the photo and size measured with *discrete* square holes method (template, sieve). Common Wolman data and photo data will have a deviation of 10% in average if the sampled area criteria are respected and data converted.

S.4.2.3 Intended purpose

None.

S.4.3 Final discussion

None

S.5 Conclusion

None

Suplementary references

Brenna, A., N. Surian, and L. Mao (2019). "Virtual Velocity Approach for Estimating Bed Material Transport in Gravel-Bed Rivers: Key Factors and Significance". In: *Water Resources Research* 55.2. Citation Key: Brenna2019a, pp. 1651-1674. DOI: 10.1029/2018WR023556.

Bunte, K. and S. R. Abt (2001). *Sampling Surface and Subsurface Particle-Size Distributions in Wadable Gravel- and Cobble-Bed Streams for Analyses in Sediment Transport , Hydraulics , and Streambed Monitoring*. Vol. 00. DOI: 10.1017/CBO9781107415324.004 PMID: 21939040. Ft. Collins, CO: U.S. Department of Agriculture, Forest Service, Rocky Mountain Research Station. DOI: 10.1017/CBO9781107415324.004. https://www.fs.usda.gov/treesearch/pubs/4580.

Bunte, K., K. W. Swingle, and S. R. Abt (2007). "Guidelines for using bedload traps in coarse-bedded mountain streams: Construction, installation, operation, and sample processing". In: *USDA Forest Service - General Technical Report RMRS-GTR*. Citation Key: Bunte2007, pp. 1-97.

Burger, W. and M. J. Burge (2016). *Digital Image Processing. An Algorithmic Introduction Using Java*. Vol. 19. Texts in Computer Science 3. Series Title: Texts in Computer Science Publication Title: European Journal of Engineering Education DOI: 10.1007/978-1-4471-6684-9 Citation Key: Burger2016a Issue: 3 ISSN: 1868-095X. London: Springer London. http://link.springer.com/10.1007/978-1-4471-6684-9.

Butler, J. B., S. N. Lane, and J. H. Chandler (2001). "Automated extraction of grain-size data from gravel surfaces using digital image processing". In: *Journal of Hydraulic Research* 39.5. Citation Key: Butler2001, pp. 519-529. DOI: 10.1080/00221686.2001.9628276.

Cerney, D. L. (2010). "The Use of Repeat Photography in Contemporary Geomorphic Studies: An Evolving Approach to Understanding Landscape Change: Repeat photography use in geomorphic studies". In: *Geography Compass* 4.9, pp. 1339-1357. DOI: 10.1111/j.1749-8198.2010.00376.x. https://onlinelibrary.wiley.com/doi/10.1111/j.1749-8198.2010.00376.x.

Church and M. A. Hassan (1992). "Size and distance of travel of unconstrained clasts on a streambed". In: *Water Resources Research* 28.1. Citation Key: Church1992, pp. 299-303. DOI: 10.1029/91WR02523.

Church and M. A. Hassan (2002). "Mobility of bed material in Harris Creek: MOBILITY OF BED MATERIAL IN HARRIS CREEK". In: *Water Resources Research* 38.11. DOI: 10.1029/2001WR000753. http://doi.wiley.com/10.1029/2001WR000753.

Diplas, P. and J. B. Fripp (1992). "Properties of Various Sediment Sampling Procedures". In: *Journal of Hydraulic Engineering* 118.7. Citation Key: Diplas1992, pp. 955-970. DOI: 10.1061/(asce)0733-9429(1992)118:7(955).

Folk, R. L. and W. C. Ward (1957). "Brazos River bar [Texas]; a study in the significance of grain size parameters". In: *Journal of Sedimentary Research*. Citation Key: Folk1957, pp. 3-26. DOI: https://doi.org/10.1306/74D70646-2B21-11D7-8648000102C1865D.

Graham, D. J., I. Reid, and S. P. Rice "Automated Sizing of Coarse-Grained Sediments: Image-Processing Procedures". In: *Mathematical Geology* 37.1. Citation Key: Graham2005a, pp. 1-28. DOI: 10.1007/s11004-005-8745-x. http://link.springer.com/10.1007/s11004-005-8745-x.

Graham, D. J., S. P. Rice, and I. Reid "A transferable method for the automated grain sizing of river gravels". In: *Water Resources Research* 41.7. Citation Key: Graham2005b, pp. 1-12. DOI: 10.1029/2004WR003868. http://doi.wiley.com/10.1029/2004WR003868.

Graham, D. J., A. Rollet, S. P. Rice, et al. (2012). "Conversions of Surface Grain-Size Samples Collected and Recorded Using Different Procedures". In: *Journal of Hydraulic Engineering* 138.10. Citation Key: Graham2012, pp. 839-849. DOI: 10.1061/(ASCE)HY.1943-7900.0000595. https://ascelibrary.org/doi/10.1061/%28ASCE%29HY.1943-7900.0000595%7D.

Hassan, M. A. and P. Ergenzinger (2003). "Use of Tracers in Fluvial Geomorphology". In: *Tools Fluv. Geomorphol.* John Wiley & Sons, Ltd. Chap. 14, pp. 397-423. ISBN: 9780470868331. DOI: https://doi.org/10.1002/0470868333.ch14. https://onlinelibrary.wiley.com/doi/abs/10.1002/0470868333.ch14.

Helley, E. J. and W. Smith (1971). "Development and calibration of a pressure-difference bedload sampler". In: *US Dep. Inter. Geol. Surv. Water Resour. Div.*, p. 21. http://pubs.er.usgs.gov/publication/ofr73108.

Ibbeken, H. and R. Schleyer (1986). "Photo-sieving: A method for grain-size analysis of coarse-grained, unconsolidated bedding surfaces". In: *Earth Surface Processes and Landforms* 11.1. Citation Key: Ibbeken1986, pp. 59-77. DOI: 10.1002/esp.3290110108.

Krumbein, W. C. (1941). "Measurement and geological significance of shape and roundness of sedimentary particles". In: *Journal of Sedimentary Research* 11.2. Citation Key: Krumbein1941, pp. 64-72. DOI: 10.1306/D42690F3-2B26-11D7-8648000102C1865D. https://doi.org/10.1306/D42690F3-2B26-11D7-8648000102C1865D.

Mair, D., G. Witz, A. Do Prado, et al. "Automated finding, segmenting, and measuring of grains in images of fluvial sediments –the potential of transfer learning in deep neural networks". In: *Submitted to Earth Surf. Process. Landforms*. DOI: 10.31223/X51H31. DOI: 10.31223/X51H31. https://eartharxiv.org/repository/view/5523/.

Mao, L., L. Picco, M. A. Lenzi, et al. (2017). "Bed material transport estimate in large gravel-bed rivers using the virtual velocity approach". In: *Earth Surface Processes and Landforms* 42.4. Citation Key: Mao2017a, pp. 595-611. DOI: 10.1002/esp.4000.

Peckarsky, B. L., A. R. McIntosh, S. C. Horn, et al. (2014). "Characterizing disturbance regimes of mountain streams". In: *Freshwater Science* 33.3, pp. 716-730. DOI: 10.1086/677215. https://www.journals.uchicago.edu/doi/10.1086/677215.

Sime, L. and R. Ferguson (2003). "Information on Grain Sizes in Gravel-Bed Rivers by Automated Image Analysis". In: *Journal of Sedimentary Research* 73.4. Citation Key: Sime1987, pp. 630-636. DOI: 10.1306/112102730630. https://pubs.geoscienceworld.org/jsedres/article/73/4/630-636/99322.

Strom, K. B., R. D. Kuhns, and H. J. Lucas (2010). "Comparison of Automated Image-Based Grain Sizing to Standard Pebble-Count Methods". In: *Journal of Hydraulic Engineering* 136.8, pp. 461-473. DOI: 10.1061/(ASCE)HY.1943-7900.0000198. https://ascelibrary.org/doi/10.1061/%28ASCE%29HY.1943-7900.0000198%7D.

Team, T. G. D. (2019). *GIMP*. Citation Key: Team. https://www.gimp.org.

Tyagi, V. (2018). *Understanding Digital Image Processing*. Publication Title: Understanding Digital Image Processing DOI: 10.1201/9781315123905 Citation Key: Tyagi2018. CRC Press. https://www.taylorfrancis.com/books/9781351342674.

Vázquez-Tarrío, D. and R. J. Batalla (2019). "Assessing Controls on the Displacement of Tracers in Gravel-Bed Rivers". In: *Water* 11.8. Citation key: vasquez2019, p. 1598. DOI: 10.3390/w11081598. https://www.mdpi.com/2073-4441/11/8/1598.

Vericat, D., R. J. Batalla, and C. Garcia (2008). "Bed-material mobility in a large river below dams". In: *Geodinamica Acta* 21.1-2. Citation Key:vericat2008b, pp. 3-10. DOI: 10.3166/ga.21.3-10. https://www.tandfonline.com/doi/full/10.3166/ga.21.3-10.

Vericat, D., F. Ville, A. Palau-Ibars, et al. (2020). "Effects of Hydropeaking on Bed Mobility: Evidence from a Pyrenean River". In: *Water* 12.1. Citation Key: Vericat2020, p. 178. DOI: 10.3390/w12010178. https://www.mdpi.com/2073-4441/12/1/178.